SIZE-DEPENDENT FILTRATION OF NON-LOADED PARTICULATE TRAPS

A Thesis

by

JESSICA KERHEANNE WHITE

Submitted to the Office of Graduate and Professional Studies of
Texas A&M University
in partial fulfillment of the requirements for the degree of

MASTER OF SCIENCE

Chair of Committee,	Andrea Strzelec
Committee Members,	Benjamin Wilhite
	Richard Malak
Head of Department,	Andreas Polycarpou

December 2014

Major Subject: Mechanical Engineering

ABSTRACT

This work investigates the filtration efficiency of uncoated, commercial Diesel Particulate Filter (DPF) substrates of three porosities (55.8%, 61.1%, 65.0%) for particulate sizes representative of Gasoline Direct Injection (GDI) exhaust, and also refines a model suitable for predicting filtration efficiency for these non-loaded particulate traps. GDI produces lower concentrations of smaller particulates as compared to diesel combustion, which results in the absence of a soot-cake and yields changes in filtration behavior compared to diesel particulate. To produce a model that simulates the filtration efficiency of non-loaded particulate traps, an existing flow field model of DPF filtration was modified to better capture the fundamental physics of deep-bed filtration. The improved model includes additional sedimentation and thermophoretic modes of filtration and the soot-cake related filtration approximations were removed. Size-dependent particulate concentrations were measured using a Scanning Mobility Particle Sizer (SMPS), both upstream and downstream of the filters. By comparing upstream and downstream particle number concentrations, the particle size-dependent filtration efficiency of filter samples was determined. Experimental results were compared to model predictions, and showed excellent agreement.

ACKNOWLEDGEMENTS

There are too many people to count that have in some way aided my work. I am humbled by the efforts and patience of so many.

My first thank-yous go to my advisor, Dr. Andrea Strzelec. Thank you for taking a chance with a graduate of mix-matched background, and for having the door open at just the right moment. The sheer good fortune of our first encounter never fails to astound me.

Further advisory thanks go to Dr. Cornelius Opris for assisting in the use of his published computational model.

I also express gratitude to Mark Stewart of Pacific Northwest National Lab for the use of the filter samples which this work intently studies, and to the Texas A&M Mechanical Engineering Department for the funding that made it possible.

Additional thanks go to the customer and technical support of TSI, particularly Maynard Havlicek who aided me through so many anxious instrumentation troubleshoots that we practically became pen-pals.

Justin Nitz, and Sherry Huang helped me with handling equipment, with taking data, and with general sanity retention efforts.

None of this work would be possible without the loving support of my family and friends. They have been comforting when presented with frustration, and demanding of the strongest possible effort on my part. They have even known when to simply let me work uninterrupted. Especially noteworthy are my mother and father for their help in formative discernment, and my grandfather for his problem solving wisdom.

This list is bookended on both sides by critical participants: the last mention goes to my beloved husband. He has made efforts and sacrifices to match mine in pursuit of this graduate degree. I would not be what I am, where I am, or who I am without Kai.

TABLE OF CONTENTS

Page

LIST OF FIGURES

Page

Page

Page

1 INTRODUCTION

Internal combustion engines are used almost ubiquitously in the developed world, and produce harmful emissions as a by-product of their combustion. Specifically, the particulate emissions have been shown to be detrimental to health; those produced by diesel engines have been shown by the World Health Organization (WHO) to cause cancer [1]. Filtration of diesel particulates has been mandated by the United States Environmental Protection Agency (EPA) for more than ten years. In diesel particulate filters (DPFs), due to particle size and aerosol concentration the particulate forms a cake of soot on the filter wall, which thereafter does the majority of filtration, quickly reaching 95% efficiency. As fuel prices increased, improvements of gasoline engines led to deployment of a technology that hybridizes the characteristics of gasoline and diesel engines; Gasoline Direct Injection (GDI). GDI engines have improved fuel efficiency compared to spark ignited gasoline engines, but also have increased particulate matter emissions. Unlike diesel engines, there currently exists no GDI particulate filtration requirement, but legislation is expected in 2015. GDI particulate both has lower particle number concentrations and smaller particle size; GDI has a particle diameter distribution peak at about 50-70nm, compared to diesel's peak at 150nm [2, 3]. Therefore, a soot cake, which does the majority of filtration in DPFs, is unlikely to form. Research to date has focused on filtration of diesel-sized particulate and has relied upon the filtration done by the soot cake. This study focuses on filtration of smaller particulate like those in the GDI size-range, in a cake free regime.

The objective of this work is to investigate the size-dependent filtration efficiency of particulate by existing cordierite substrates as a function of porosity and flowrate, and to refine an existing filtration model for use with cakeless filtration.

2 LITERATURE REVIEW

2.1 GDI Particulate

Work by Maricq at Ford has yielded information about both the size and number concentration of particle matter from several types of engine technologies [2]. Figure 1 illustrates the size ranges and concentrations of particulate emissions from several different fuels and engine technologies.

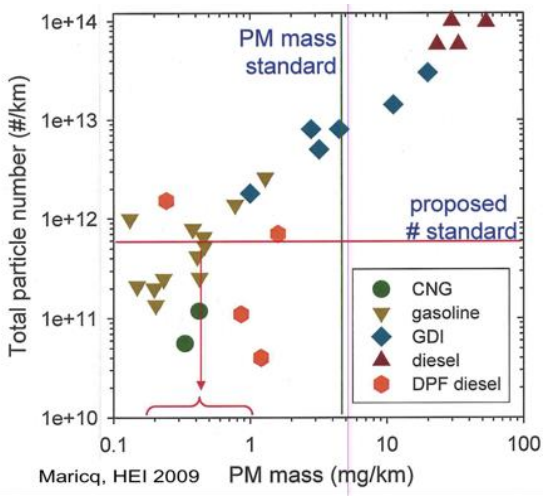

Figure 1–Particulate emissions of several engine technologies and fuels [2].

In DPFs, particulate matter quickly forms a cake layer on the channel walls of the filter. Thereafter this cake does the majority of the filtration, and the filter soon reaches 95% filtration efficiency or greater. Since GDI particulate both have lower number concentration and are

smaller than diesel particulate (see Figure 1), a soot cake is unlikely to form. **Thus, the filtration of GDI particulate will be a function of the substrate rather than of the soot cake.**

In 2012, the World Health Organization (WHO) determined that diesel exhaust particulates are carcinogenic, especially in the lungs and airways [1]. Work from Heyder [4] shows that smaller particulate such as those found in GDI exhaust particulates penetrate more deeply and deposit in the fine airways; the bronchioles and the alveoli, as illustrated in Figure 2. Furthermore, exposure to fine particulate from automotive exhaust is associated with an increase in adverse cardiovascular events, such as myocardial infarction, heart failure, and stroke [5]. Therefore, GDI particulate emissions represent a significant health risk.

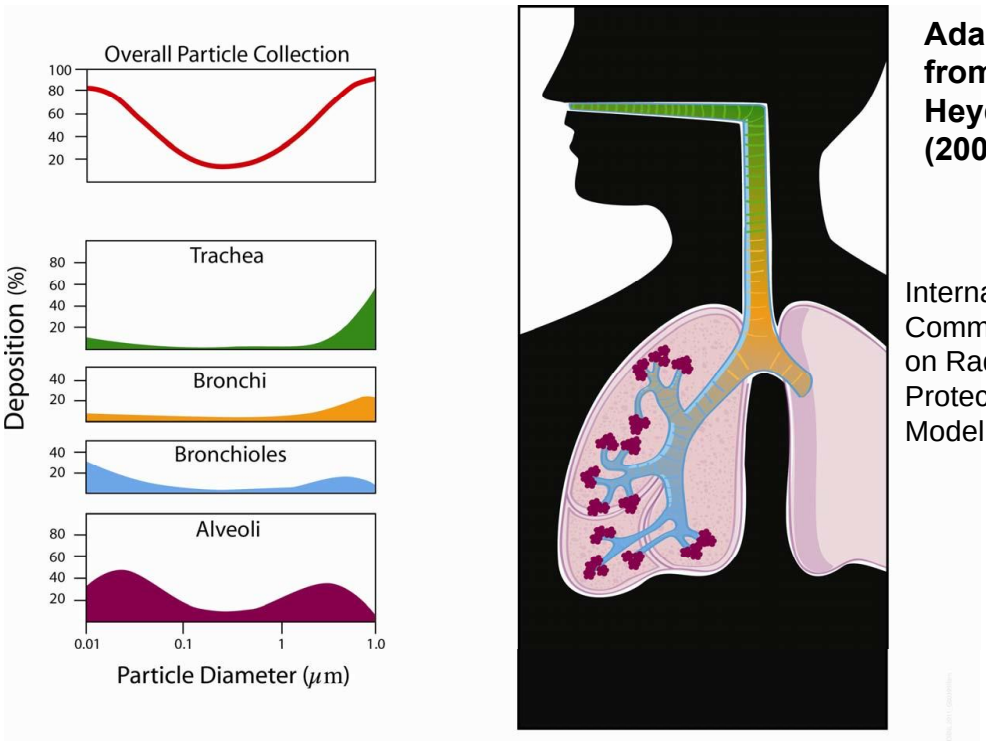

Figure 2 – Deposition of fine particulate in the lungs and airways.

2.2 Diesel Particulate Filters

Diesel Particulate Filters (DPFs) have been engineered to simultaneously meet competing requirements. The filters must efficiently remove particulate from the exhaust, but the filter must not cause a restriction of the exhaust stream that unacceptably impacts the engine's performance. Particle laden flow enters the substrate and is mechanically filtered by the channel walls. As shown in Figure 3, particulate matter quickly forms a cake layer which becomes responsible for the majority of the filtration. As gas flows through a porous media, the flow experiences a pressure drop which is described by the Darcy equation (26). This pressure drop has an adverse effect on engine performance, and increases as the filter further fills with soot. The filter eventually requires regeneration to remove the built up particulate, reduce the additional pressure drop caused by the soot cake, and prevent impacting the engine's performance.

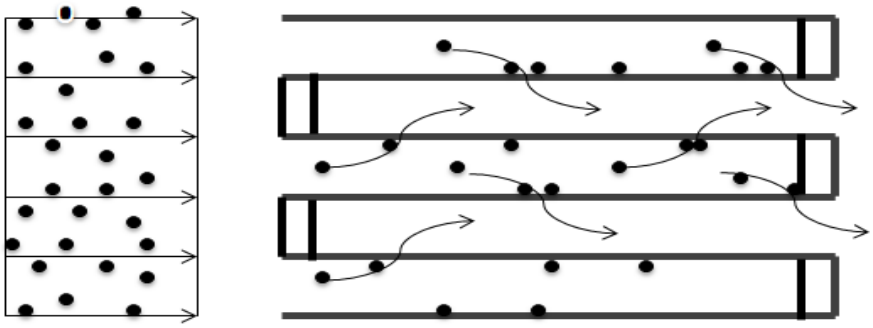

Figure 3 - Illustration of flow through a DPF channel wall

The first published works on DPFs appeared in the 1980's [6]. Early research focused on filter design, including porosity and cell geometry performance effects. Increased porosity of cordierite filters did not necessarily decrease the pressure drop, as demonstrated by Merkel at al. [7]. While it was found that filter backpressure was not a reliable indication of the extent of filter loading [8], it was still known that increased backpressure resulted in reduced engine

performance [9] [10]. These works all investigated filtration by substrates with a soot cake, and neglect the cakeless regime.

Investigation on the impact of porosity and cell geometry on backpressure of cordierite filters was done by Hashimoto et al. [11]. Increasing the porosity from 53% to 59% and average pore diameter from 15 to 25um gave a 20% decrease in pressure drop. Modifying cell density to minimize pressure drop delivered another 40% reduction. These modifications did not affect filtration efficiency, because the majority of the filtration in DPFs is done by the soot cake and not the filter walls. This study did not address the filtration efficiency of clean filters.

Studies have additionally been done on the effect of pore size distribution on filtration [12] [13] [14] [15] and on DPFs of material other than cordierite, such as aluminum titanate [16] [17] [18] [19], silicon carbide [20] [21], and mullite [22]. However, no specific study was made of deep bed filtration for any of these materials.

Currently DPFs surpass the United States Environmental Protection Agency's (US-EPA) particulate emission filtration requirements. A 2013 publication [23] showed that engines fitted with DPFs produce 16 mg/(kW hr), well below the mandated 20 mg/(kW hr) limit by regulation.

2.3 Filtration Models

The initial fundamental work was done on the study of filtration by packed beds in the 70's by Cookson and Payatakes. Cookson's interest was in removing the virus E. coli using packed beds of activated carbon. A sensitivity study was done by varying the physical characteristics of the packed beds employed, and from this study a model of removal efficiency based on the physical parameters of the system was presented. The model was based on particle transport by Brownian diffusion, and was used to predict the effect of bed height, porosity, fluid flow rate, and bed grain size on filtration [24]. Brownian diffusion is the random motion of particles in a fluid due

to collisions with other atoms or particles. Filtration due to Brownian diffusion occurs when a particle is moving past a grain of the packed bed and is intercepted due to the particles movement within the stream. However, for this model the particle-laden fluid was water rather than gas.

Payatakes developed a model for flow in a packed bed of monosized spheres (grains), with the intention that this model be used to predict the rate of particulate deposition in a packed bed. This type of filtration is known as deep-bed filtration. By assuming the bed consisted of perfect spheres of a single diameter, the bed's void spaces could be considered as a number of unit cells of identical shape and dimension, connected in parallel. The shape of these voids was of a short length of tube with a constriction in the center. Flow through a network of such voids was mathematically shown to be approximately equal to flow through a single long tube with periodic constrictions. The flow model was validated by comparing modeled friction factors to experimental for two beds of different parameters [25]. The approximation of filters as a backed bed of spheres is a common theme that can still be seen in filtration models employed currently. However, this model cannot be directly used for the filtration of GDI particulate because it employs liquid instead of gas as the fluid to be filtered. Use of gas instead of liquid did not occur until the work of Lee.

Lee employed the Kuwabara model [26] of forces on a multiplicity of spheres in a viscous fluid to model the filtration of aerosol particles from gas by a packed bed. This model encompassed Brownian diffusion and interception modes of filtration that were derived by using boundary layer behavior to account for the effect on flow of neighboring spheres in the packed bed. Direct interception filtration occurs when a particle intercepts a grain of the packed bed and sticks to it, and is thus removed from the fluid flow. These two effects are assumed to be additive. However,

the experimental data compared to the model exist in the range where diffusion is the dominant filtration mode. Therefore, the model is insufficiently validated [27].

The model of the filtration of aerosol by granular media by Pendse is based on the constricted tube model, and accounts for both the diverging and converging behavior of the flow in porous material and interference due to neighboring grains. Particle trajectories are used to determine filtration efficiency. This model assumes first that the aerosol particles are distributed randomly in the flow stream, second that any interception between a particle and a collector grain results in a guaranteed particle deposition, and third that collected particles thereafter behave as collectors. This leads to the formation of aggregates of deposited particle. However, the model does not account for the change of the flow due to these deposits, and therefore does not capture the change in filtration behavior of a filter over time [28].

The study of modeling the honeycomb wall-flow DPFs began with the work of Bissett and Shadman in the 1980's. A mathematical model of DPF regeneration was produced by defining a system of nonlinear partial differential equations to describe the conservation of mass, energy, and momentum [29]. The solution to this system was numerical, and achieved through use of finite difference and finite element techniques for spatial discretization, and by employing an implicit ordinary differential equation solver for the resulting time integration. The work was later refined to show four separate stages within the regeneration: preheating, ignition, combustion, and cooling [6]. The focus of this model was to determine peak temperature and the total regeneration time, as the former may cause melting in the DPF while the latter determines the extent of particulate removal from the filter by regeneration.

Some of the most robust models of DPFs were published by Konstandopoulos and Johnson in 1989 [30]. The model assumed the DPF to be an isothermal, perfectly packed bed of spheres at

steady-state, and included both Brownian diffusion and direct interception modes of filtration. The steady-state assumption effectively neglects the loading phase of the filter, when deep-bed filtration is dominant because a cake has not yet formed. While the model was in good agreement with the experimental data for particulate larger than 1um diameter, it did not correctly predict the filtration behavior at smaller particle diameters. To justify this finding, the paper concluded that smaller particulate were being produced downstream of the filter.

In 1998, continuing research by Opris and Johnson developed a two dimensional model of filtration as a function of particle size that describes the flow field of the filter. The filtration efficiency was formulated as a function of wall thickness, gas velocity, temperature, and porosity of the filter. The model utilized the previously seen Brownian diffusion and direct interception modes of filtration, as well as filtration due to inertial impaction. This model agrees well with experimental data, including particulate larger than 1um in diameter, with no need for empirical fitting parameters [31]. This model includes Brownian diffusion, direct interception, and inertial impaction modes of filtration. Even though this model focuses on cake filtration, it includes terms for deep-bed filtration and can therefore be modified to simulate cakeless filtration.

Pontikakis et al continued the pattern of studying filters as a multitude of collecting units, with the additional complexity that the collectors were assumed to be cylindrical instead of spherical [32]. This modeling effort was directed towards foam filters, which have a pore structure of twelve-sided polyhedrons. The struts between each pore are the cylindrical collectors being modeled. The model attempts to simulate the dynamic behavior of the filter by accounting for the filtration of “blocked passages” as the filter fills. Brownian diffusion, direct interception and inertial impaction modes of filtration are accounted in the model, which assumes that the foam is comprised of identical pores. Because this assumption is not valid, an experimentally determined

fitting parameter was introduced to correct for deviations in the foam structure. Since this fitting parameter is expected to vary from sample to sample due to the variability in the foam structure, and since it cannot be determined except by testing each sample, this model cannot be easily applied to filters in general.

Liu and Miller developed a flow model of wall-flow filters with equilateral triangular channels, rather than the conventional square channels [33]. However, since this filter design was never widely commercially implemented, the model remains unused.

Huynh et al. developed a one dimensional "two layer" computational model to simulate both the filtration and regeneration of a DPF [34]. The model assumes the filter is a packed bed of spheres, but includes only Brownian diffusion and direct interception effects in its filtration calculations. Filter permeability was calculated from empirical correlations by measuring the pressure drop across the clean filter, and was then used as an input to the filtration model. Since this model does not include physics of inertial impaction, we chose not to use it as a basis for the model developed in the present work.

Marre et al developed a filtration model concerning filters composed of sintered grains [35]. This model first approximates the disorderly grains as a cubic lattice, and then models the resulting discrete cylindrical pore network. The efficiency as a function of particle size is determined analytically, based on the efficiency of cylindrical pores. The model focuses on submicron particle filtration, and accounts for Brownian diffusion and direct interception modes of filtration, but neglects other modes employed in previously published literature.

Sbrizzai et al. presented a model of filtration calculated with computational fluid dynamics [36]. The model tracks the motion of "large swarms" of particles to determine particle deposition using a finite-volume Navier Stokes solver. The permeability of each filter sample was

determined by fitting experimental data to the Ergun equation. The rate of particle deposition was determined from rarefied gas theory and bounce/capture models. Brownian motion is included in the equations of motion of the particles. In addition to this model being computationally intensive and semi-empirical, the only particle diameters studied were 2um and .2um. This model does not consider the polydespersity of the particulate being filtered. Since filtration efficiency varies with particle diameter, this model is insufficient for the goal of simulating the filtration efficiency of GDI particulate.

Ohara et al. have presented an analytic model of filtration efficiency, based on the spherical collector model, which accounts for Brownian motion, direct interception and inertial impaction but neglects other modes of filtration. The model was validated against experimental data gathered with an SMPS system, using Zn_2Cl particles generated by an atomizer. However, this experimental data mimics the distribution profile of diesel particulate emissions, rather than the GDI-like conditions studied in this work [37].

Similar to that of Sbrizzai, Liu et al. have independently developed a filtration model based on particle trajectories [38]. This model tracks the motion of numerous quantities of monosized particles, and accounts for drag force, Brownian motion, and partial slip flow. As before, this model is computationally intensive and can only consider one particle diameter at a time. Furthermore, this model does not consider the efficiency of a clean filter, and therefore is not useful for modeling the filtration of GCI particulate.

A computational fluid dynamics model was developed by Bensaid et al. to simulate pressure drop, and filter loading along the length of a filter channel [39]. The filtration model is based on spherical collectors, and accounts only for Brownian motion and direct interception modes of filtration. Simulations were run at a variety of flow rates, filter permeabilities, and particle

diameters. While the model shows that filtration efficiency changes with particle size, it does not produce a function of filtration efficiency versus particle size. This is because the model can only consider one particle diameter per simulation. The authors conclude that filters over time will tend towards a nearly constant soot cake layer thickness, and that the most penetrating particle size lies somewhere between 200 and 500nm. Since the case of clean filter efficiency is not considered, and since it fails to account for polydispersity, this model is not useable for simulating the filtration of GDI particulate.

Tandon et al. have produced a model of filtration efficiency as a function of soot loading which accounts for Brownian diffusion, direct interception, and inertial impaction [40]. The model was used to examine the sensitivity of filter efficiency on pore diameter and porosity, flow rate, fluid temperature, and aerosol properties. This work considered clean filter efficiency and pressure drop as a transitory case only, and focused on loading of the filter. Dependence of filtration efficiency on particle size was not studied.

Wang et al. have investigated deposition of polydisperse particulate due to thermophoresis, agglomeration, and turbulence. These effects were studied on the channel level, rather than between grains of a packed bed. The authors derived an expression for thermophoretic deposition and validated it against experimental data. This expression compared favorably to others in the literature. Deposition due to agglomeration and turbulence were both found to be negligibly low [41].

2.4 Summary

Previous research of automotive exhaust particulate emissions filtration has focused on filtration of diesel exhaust. Mandated filtration of diesel exhaust has been in place for more than a decade, yet there are currently no requirements for the filtration of gasoline particulate emissions. Since

these particulates represent a significant health hazard, it is likely that these emissions will come under regulation in the near future.

DPFs strongly rely on the built up soot cake to filter particulate from the exhaust stream. However, since GDI particulate emissions are both lower in concentration and smaller than diesel particulate emissions, a soot cake is not likely to form, and the filter will rely more on deep bed filtration of the filter walls. Computational models of DPF filtration focus on the filtration done by a filter's soot cake. Thus, models of GDI particulate filtration will need to shift attention from soot cake filtration to deep bed filtration.

This work evaluates and models the filtration behavior of existing filter substrates under GDI-like conditions.

3 EXPERIMENTAL SETUP

This study examines three porosities (55.8%, 61.1% and 65.0%) of uncoated cordierite filters, with inlet cell densities 200 CPSI, 300 CPSI, and 200 CPSI respectively. As shown in Figure 4, the filters have a checkerboard arrangement, with half the cells plugged by impermeable material on the front face and the other half plugged on the reverse face. The porous material mechanically removes particulate matter which slowly accumulates and blocks the pores, thereby increasing filtration efficiency.

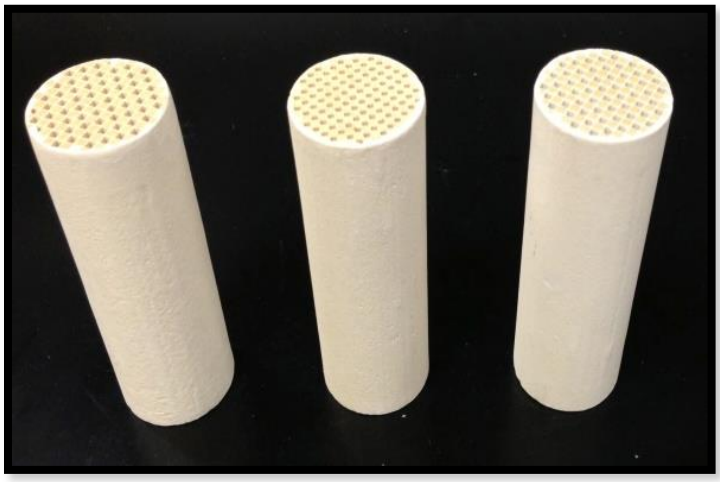

Figure 4 - Cordierite, wall-flow filter samples. From left to right, the samples have porosities of 55.8%, 65.0% and 61.1% and cells per square inch of 200, 300, and 200 respectively. The filters are 76.4 mm long and the filter walls have thickness of 0.3 mm (12 mil).

Particle laden flow travels axially down the length of a channel and is forced to pass through a filter wall by the impermeable plugs before exiting the filter, as described previously and shown in Figure 3.

The particle emissions of diesel engines are the result of incomplete combustion of fuel. They consists of mostly black carbon with some attached hydrocarbons [42]. The soot particles have fractal shape and include chains that are approximately 50–150 nm in diameter. These chains are agglomerates composed of smaller units, called primary particles, that are about 5–20 nm in diameter. Mobility diameter is related to the size, shape and orientation of particles [43]. In filters, aspherical particles may or may not become collected based on their alignment. Furthermore, the size distribution and composition of real soot particles is affected by the engine operating conditions, and even atmospheric conditions. This makes the study of DPF filtration efficiency with real diesel soot particles difficult, and necessitates the use of simpler, more reproducible particulates. Studies of filtration efficiency and simulations have been conducted by multiple researchers, see section 2.3. In these models, the simulated particles were assumed to be spherical with diameters similar to those of the mobility diameter of real soot agglomerates. Mobility diameter is determined by using an electrostatic field to parse particles by charge to mass ratio, see section 3.2.3. For the experiments in this work, salt particulate were used rather than soot because the particle size distributions are reproducible, and the particulate dissolve easily in water when regenerating the filters [44].

Salt particulate were generated by atomizing (Model 3076) a 0.025 M solution of ammonium sulfate. The resulting colloidal mixture was then passed through gas drier beds in series for dehydration. The peak of the particle size distribution generated by a 0.025M solution of ammonium sulfate lies at ~70 nm, which is in the size range of GDI exhaust particulate matter. The complete salt concentration distribution characterization is given in the appendix.

Particle size-dependent filtration efficiency of samples was measured by a Scanning Mobility Particle Sizer (SMPS; TSI Inc., DMA Model 3080 and CPC model 3787) following a modified

protocol similar to [42]. The experimental setup, shown in Figure 5, was configured to sample from either upstream or downstream of the filter sample. By comparing the particle counts as a function of particle diameter for these two locations, the size-dependent filtration efficiency was determined.

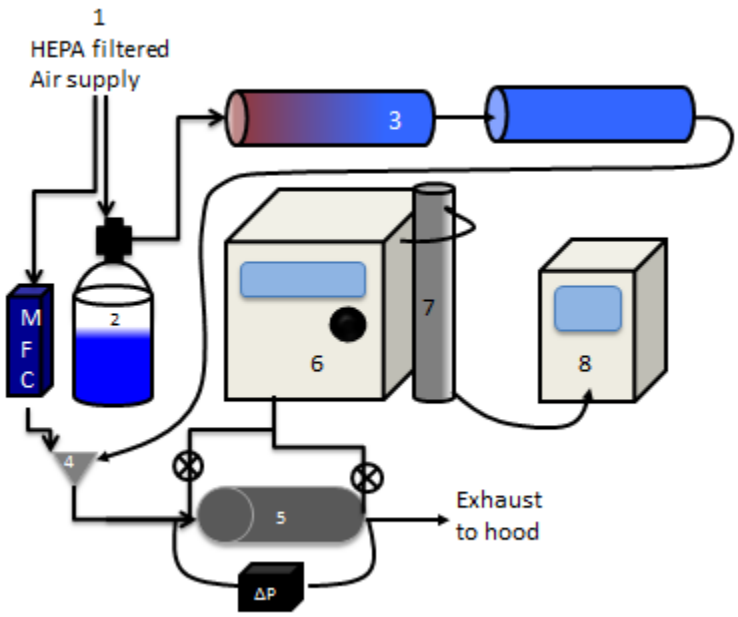

Figure 5 - Diagram of experimental setup. Filtered building air passes through an atomizer of ammonium sulfate solution (1) and the mist created is dried by a pair of diffusion driers (3). Make up air moves through a mass flow controller (2) which is used to select the flowrate the filters are tested under. Dry, particle laden flow then moves to the filter (4). A pressure transducer (5) measures the change in pressure across the filter. Polydisperse flow is selected based on electromobility by a classifier (6), and the aerosol concentration is measured by the condensation particle counter (7). Valves upstream and downstream of the filter allow the setup to measure particle counts before and after the filter. Comparing upstream and downstream yields the filtration efficiency as a function of particle diameter.

Filtration efficiency experiments were conducted on three cordierite filter samples each of porosity 55.8% (200 CPSI), 61.1% (300 CPSI) and 65.0% (200 CPSI). Each filter sample was

tested in a fresh, never before used state, and in post-regenerated state. As shown in the appendix, we observe differences between the filtration behavior of the fresh and post-regenerated filters. The post-regeneration experiments were replicated for statistical analysis. Samples were examined at multiple time points; hour 0, hour 1, hour 2 and hour 3. One additional extended experiment of eleven hours was also conducted on one sample of each porosity, to investigate possible cake formation. Between experiments, filters were washed for six hours in a heated and sonicated bath of deionized water (changed hourly), and dried in a vacuum oven.

3.1 Particle Generation via Constant Output Atomizer

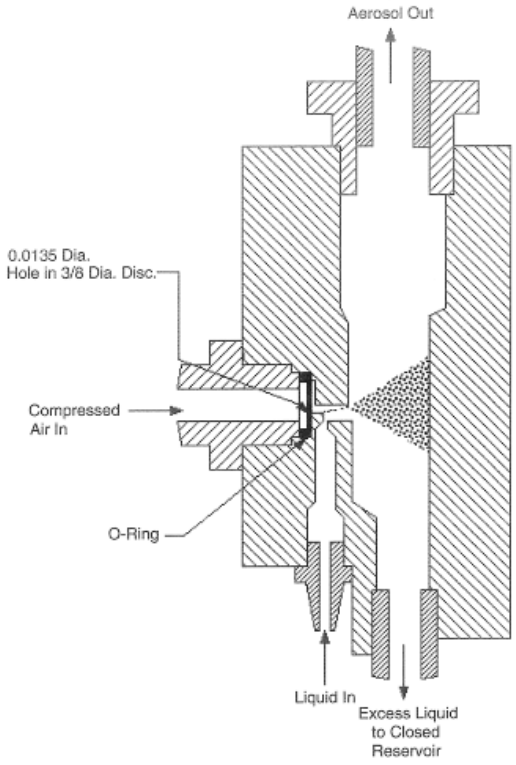

Figure 6 - The constant output atomizer assembly block [45]

The constant output atomizer is a TSI model 3076. A diagram of the atomizer assembly block is given in Figure 6. Compressed air passes through an orifice and expands to form a high-velocity jet. Liquid is drawn from the glass solution container into the atomizing area through a thin, vertical stainless steel tube and is then atomized by the jet of air. A fine mist of water droplets and salt exits the atomizer through the top of the atomizer assembly block, and passes to a pair of gas drier beds for dehydration. Large droplets are removed by impaction with the opposite wall and the resulting excess fluid drains from the bottom of the assembly block to the solution container [45]. A metered valve at the inlet of the atomizer initiates or terminates flow into the atomizer and thus controls the production of aerosol.

3.2 The Scanning Mobility Particle Sizer

3.2.1 The Classifier

The electrostatic classifier is a TSI Series 3080, and size-classifies monodisperse, submicrometer aerosols in the particle diameter range from 10 to 1000 nanometers. The classifier parses particles by diameter for measurements of particle size distribution. Monodisperse aerosol exiting the classifier passes to the condensation particle counter (CPC), which measures particle number concentration. By scanning through bins of particle sizes, the SMPS measures the size distribution of the aerosol.

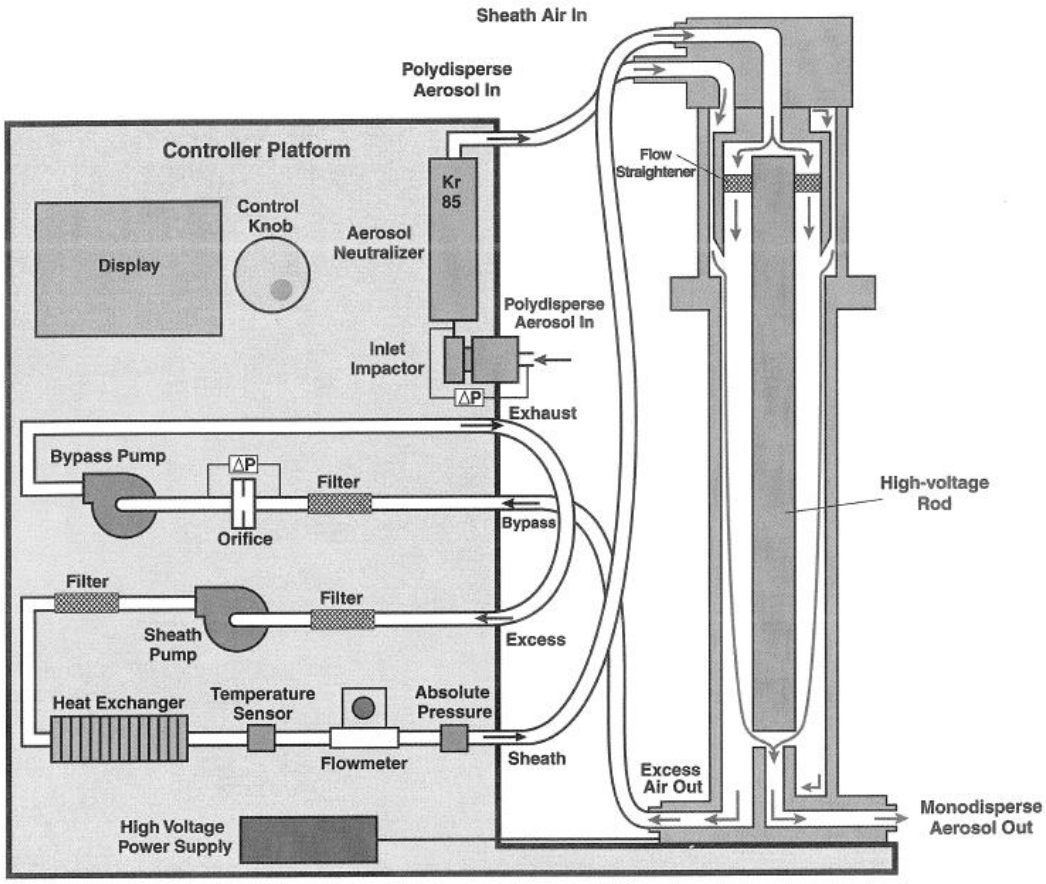

Figure 7 - A Diagram of the electrostatic classifier [46]

The classifier consists of several subsystems, shown in Figure 7, that are needed to provide a monodisperse output to the CPC. These include the impactor, the sheath-air flow controller, the aerosol neutralizer, the high-voltage controller, and the differential mobility analyzer.

The impactor is mounted outside the inlet to the classifier, and removes particles above a known size by inertial impaction. The flow passes through a nozzle and is then forced to make a sharp turn. Large particles with high inertia leave the stream and intercept a removable steel plate. This plate and the nozzle are routinely washed and carefully dried to prevent salt buildup and subsequent disruption of the aerosol stream.

The sheath flow controller maintains a constant flow through the sheath flow loop. This loop consists of a filter, a pump, a filter heat exchanger and a flow meter. The flow meter has built-in temperature and pressure sensors. The flow is monitored by a microprocessor and used to control the pump based on the desired flow rate which is input from the front panel of the classifier. For all the experiments listed here, the sheath flow rate was set to 3.0 lpm.

The high-voltage controller provides a charge on the center rod that acts as an electrode for the differential mobility analyzer. The voltage is monitored by a sensitive high-voltage divider and managed by a microprocessor. As the classifier scans through the desired range of particle sizes, the high-voltage controller changes the voltage of the electrode to select the correct electrical mobility, and thus the correct particle diameter [46].

3.2.2 The Aerosol Neutralizer

The aerosol neutralizer is a Model 3087 made by TSI, and is designed to neutralize electrostatic charges on aerosol particles as they pass through the device. The energy of x-rays lies between 0.12 and 120 keV, soft x-rays range from 0.12 to 12 keV. Our aerosol neutralizer generates x-rays in the energy range of 3 to 9.5 keV, with the majority of the waves at 8.4 keV [47]. These soft x-rays ionize gas molecules in the aerosol chamber to create both positive and negative ions. These ions are attracted to and will neutralize oppositely charged particles. The sample stream exits the neutralizer as polydisperse flow and forms one of the inlets to the differential mobility analyzer, which then manipulates the remaining charged aerosol particles [47].

3.2.3 The Differential Mobility Analyzer

The Differential Mobility Analyzer (DMA) is mounted onto and controlled by the classifier. When the classifier scans through the particle diameter range of interest, it is the DMA that parses and selects each diameter bin in turn. A diagram of the DMA is shown in Figure 8. The

DMA comprises two polished stainless steel cylindrical electrodes which are insulated from each other by a Teflon annulus at the top and an acetyl-plastic annulus at the bottom. The lower insulator allows enough voltage leakage to prevent a static charge buildup near the exit.

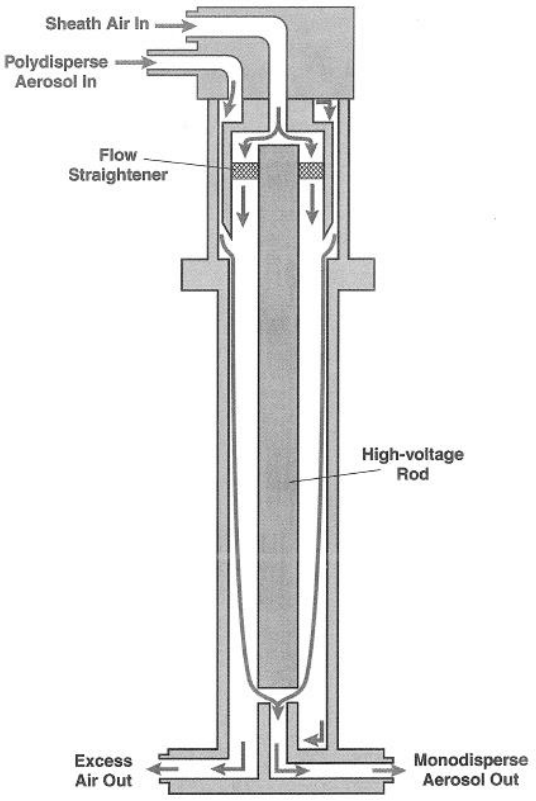

Figure 8 - The differential mobility analyzer [46]

Filtered air enters the sheath flow inlet of the DMA and passes to and annular chamber at the top. The flow is made laminar by travelling through a double screen of nylon mesh. The air flows downward axially and through a region of electric field for classification. Polydisperse

flow enters the DMA through an inlet at the top and passes through a narrow annular gap to evenly distribute the concentration of particles. The thin annular flow travels to the classification region and is merged with the laminar sheath-air flow.

Particles with positive charge are attracted to and eventually intercept the outer electrode. Neutral particles are unaffected by the field, and are removed with the excess flow. Negatively charged particles are attracted to the inner electrode as they move downward along the length of the DMA. Particles with a narrow range of electrical mobility may enter one of twelve apertures that are equal in size and location along the center electrode. These exit the DMA as monodisperse flow, and are passed to the condensation particle counter [46].

3.2.4 The Condensation Particle Counter

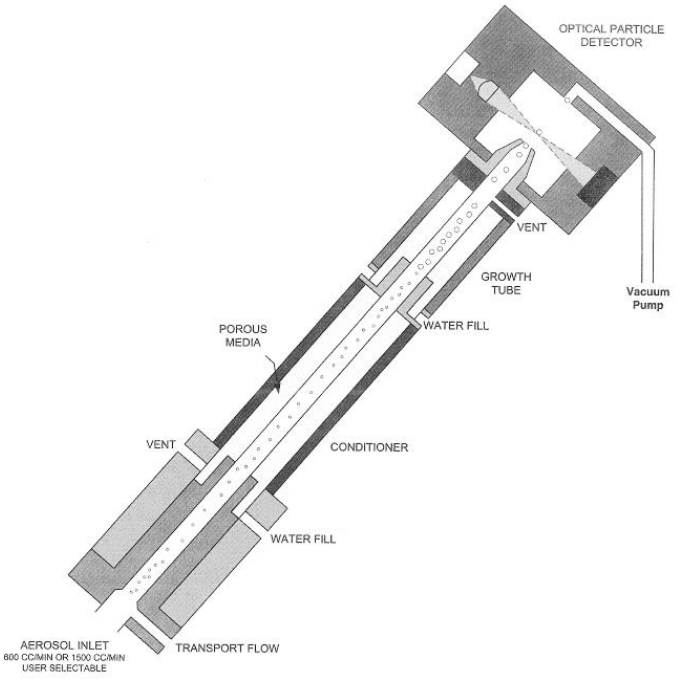

Figure 9 - The growth tube of the condensation particle counter [48]

The CPC is a Model 3787 made by TSI. The growth tube of the CPC is shown in Figure 9. The aerosol stream enters the sample inlet at either 0.6 lpm or 1.5 lpm. The higher flow rate was used in these experiments, to reduce particle loss. The aerosol passes to the conditioner, where the sample stream is saturated with water vapor and equilibrated for temperature and humidity. The stream then passes to a growth tube where the walls are wetted walls to increase the vapor pressure. Water's high diffusivity allows the vapor to permeate sample stream faster than the air stream can be heated by the walls. Water is thereby caused to condense on the sample particles. A viewing volume of the enlarged droplets are illuminated by a laser and detected by an optical sensor. A pulse of light from each particle is converted to an electrical signal and processed by the CPC's electronics [48].

The instrument interfaces with a laboratory computer via TSI's Aerosol Instrument Manager software (AIM). For these experiments, we use the software's option to collect data of particle number concentrations, in cm-1 units, as a function of particle diameter. These data are passed to AIM for exportation and later analysis.

4 RESULTS & DISCUSSION

The hourly filtration efficiency of 55.8% porosity (200 CPSI) is plotted in Figure 10. Evidence of the beginnings of cake formation can be seen between hours four and six, and the filter approaches a fully loaded state in eleven hours. The pressure drop increases slowly as a function of loading. The filtration efficiency increases most in the first four hours of observation, and continues increasing more slowly after the fourth hour. The consistent, monotonic increase in filtration efficiency is what we'd expect as the filter walls accumulate particulate. The same is true for the pressure drop; it is expected to trend generally upward with loading.

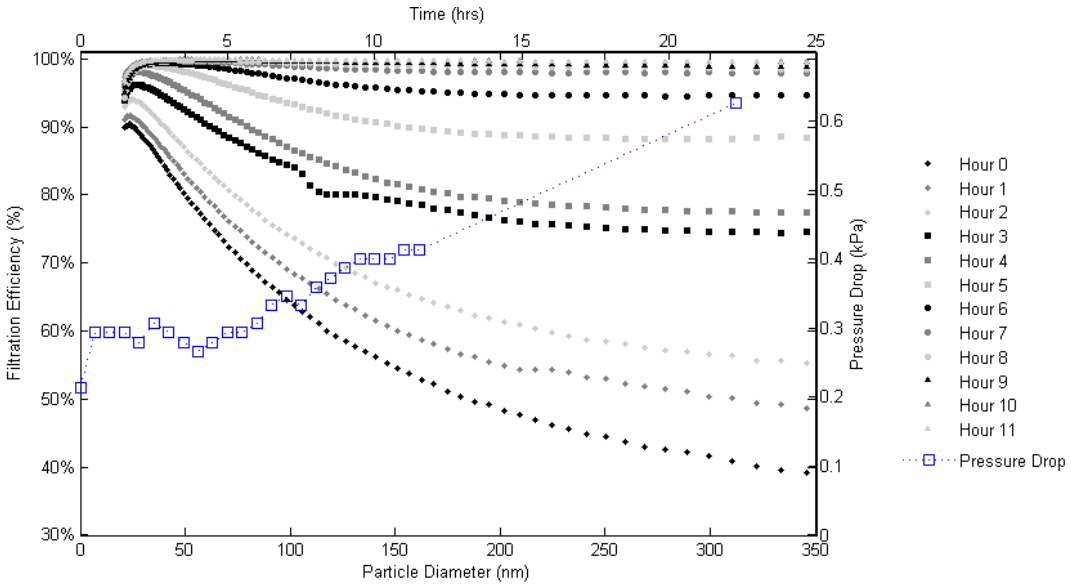

Figure 10 - Filtration efficiency and pressure drop of 55.8% porous filter as a function of time

The hourly filtration efficiency of 61.1% porosity (300 CPSI), given in Figure 11, showed indications of the beginning of cake formation between hour five and hour eight, and approached

fully loaded at hour eleven. The pressure drop was lower overall than the 55.8% porosity, and increased over time more slowly than the 55.8% porosity as expected.

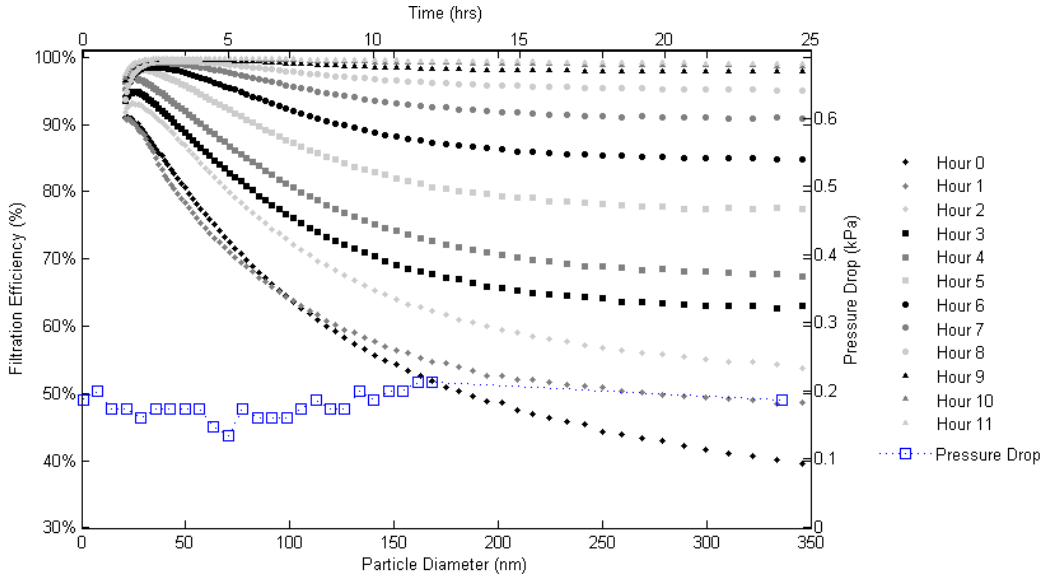

Figure 11 - Filtration efficiency and pressure drop of 61.1% porous filter as a function of time

The results of the twelve hour test of a 65.0% (200 CPSI) filter sample are given in Figure 12. The filtration efficiency increased with each hour, but the filter did not reach mature cake filtration by hour eleven. Pressure drop increases more slowly than the 55.8% and 61.1% porosities.

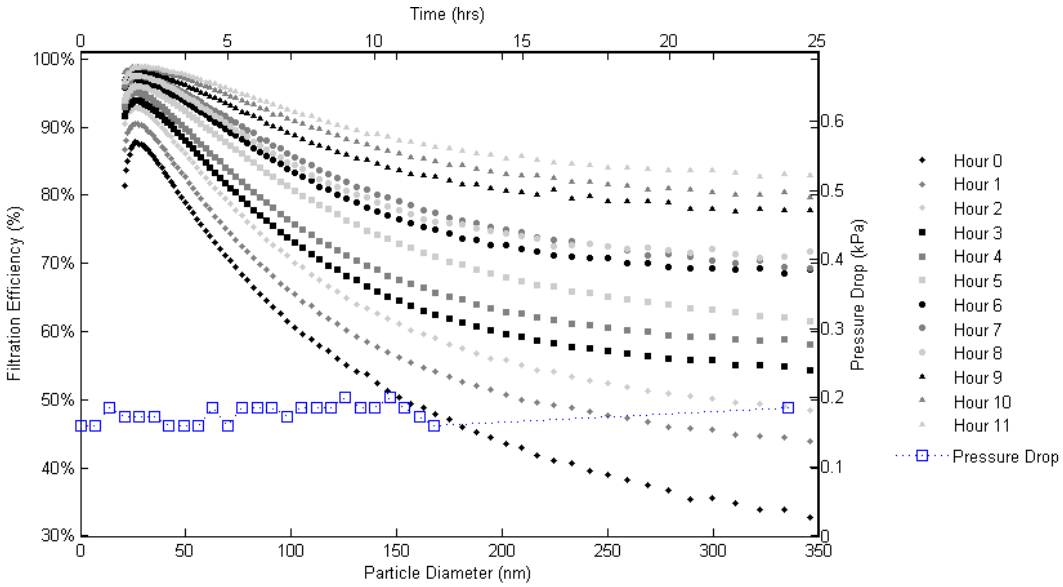

Figure 12 - Filtration efficiency and pressure drop of 65.0% porous filter as a function of time

This work focused the first four hours of filtration, with replicates on each sample of each porosity at two flowrates. The filtration efficiency at hour 0 for all porosities are shown in Figure 13 and Figure 14. At 15,000 hr^{-1}, the filtration efficiency of the 65% porosity is lower than that of the 55.8% porosity. The 61.1% porosity does not fall between 55.8% and 65.0%, due to its greater number of inlet cells per square inch. This results in a lower surface velocity at the filter wall, which increases filtration efficiency.

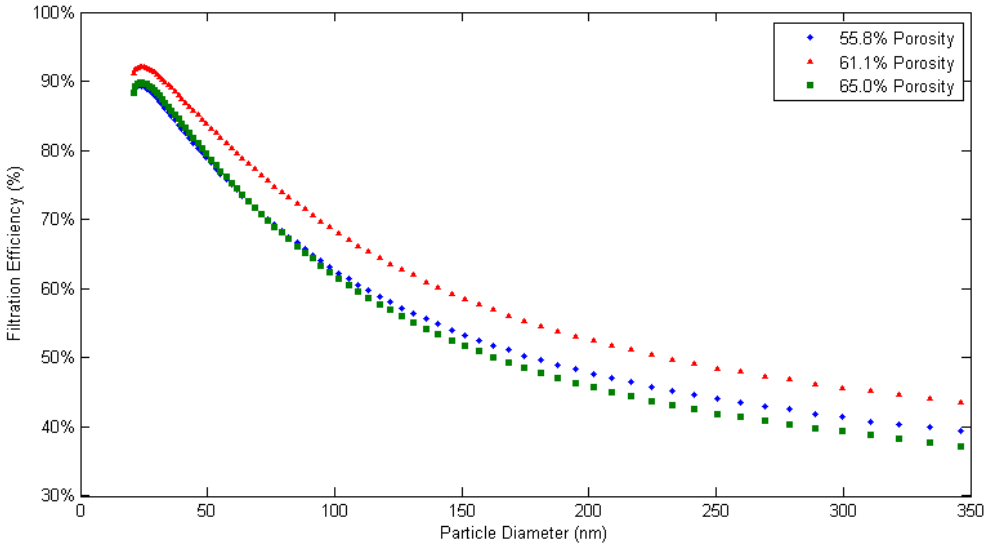

Figure 13 – Effect of porosity on filtration efficiency at 15,000 hr-1

To verify that the cells per square inch caused the ordering of filtration efficiencies seen experimentally, simulations of filters that have consistent cells per square inch were run at 15,000 hr^{-1}. Figure 15 shows the result. The filtration efficiencies increase with decreasing porosity, where previously the filtration efficiencies were not ordered with porosity.

The filtration efficiency of the 65.0% porosity (200 CPSI) is lowest, and that of the 61.1% porosity (300 CPSI) is highest when the filters are tested at 30,000 hr^{-1}. Filtration efficiencies for all porosities are reduced at this higher flowrate. This also supports the conclusion that higher velocity of the gas across the filter wall causes reduced filtration efficiency.

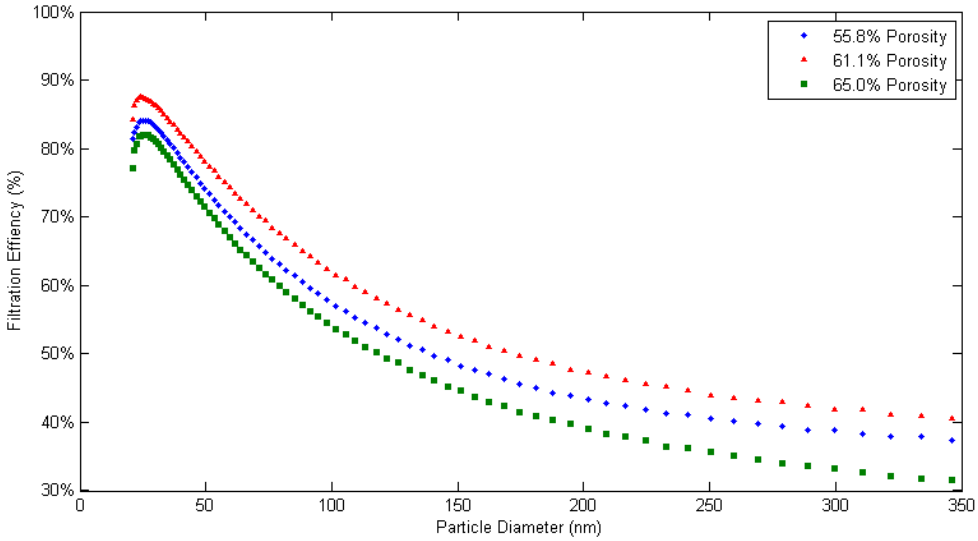

Figure 14 - Effect of porosity on filtration efficiency at 30,000 hr-1

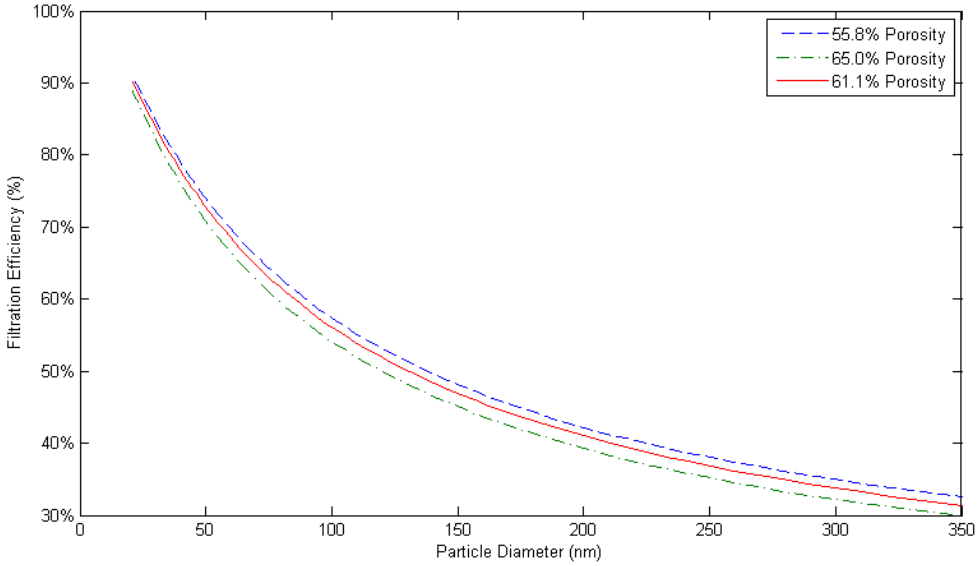

Figure 15 - Simulated filtration efficiencies with constant CPSI at 15,000 hr-1

Figure 16 compares the filtration efficiencies of 55.8% (200 CPSI) porosity at 15,000 hr^{-1} and 30,000 hr^{-1}. As expected, increased flow rate decreases filtration efficiency. This plot is representative of the reduction in filtration efficiency with increased flowrate observed for all porosities, see appendix.

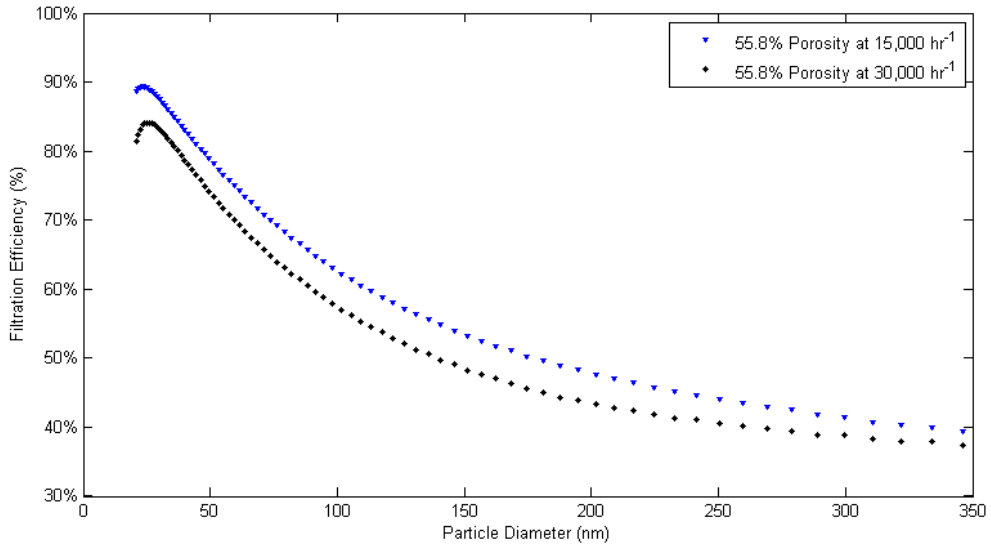

Figure 16 - Effect of flowrate on filtration efficiency for 55.8% porosity

According to Darcy's Law, changes in the pressure drop across the filter are due to changes in the permeability of the filter as it fills with particulate. Parameters such as flowrate also affect the permeability of the filters. Figure 17 shows that permeability of the filters decreases with flowrate and with loading.

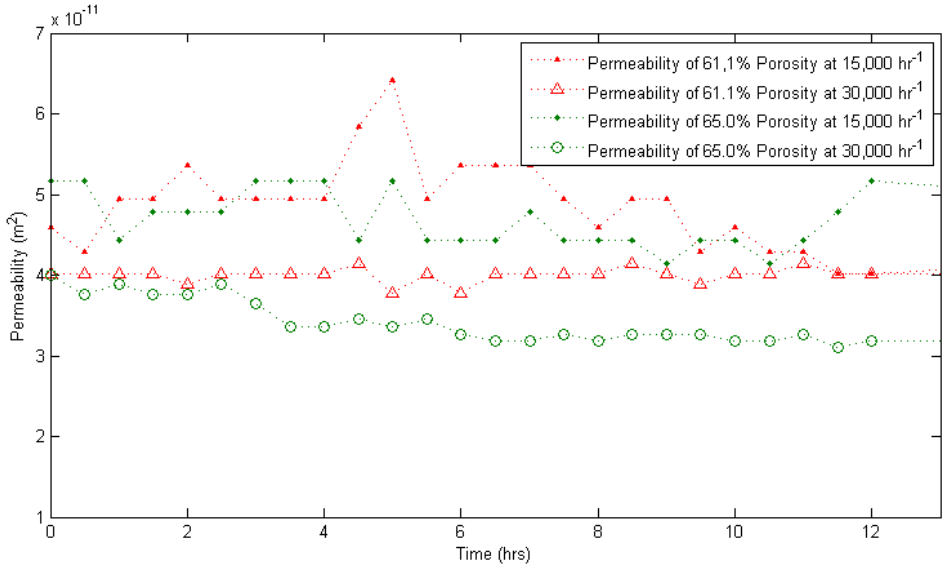

Figure 17 - Effect of flowrate on permeability for 61.1% and 65.0% porosity

Figure 17 demonstrates the decrease in permeability with loading and increased porosity. Filters have higher permeability at lower flowrate as expected. However, the 61.1% porous filters have a higher permeability than the 65.0% porosity. This is another effect of the filters' CPSI; the lower surface velocity of the 300 CPSI filters increases the permeability. The decrease in permeability as flowrate increases is more pronounced for the 55.8% porosity than for the 65.0% porosity, as it fills more quickly with particulate. Figure 18 compares filters of the same CPSI and shows that permeability increases with increasing porosity, where CPSI is held constant.

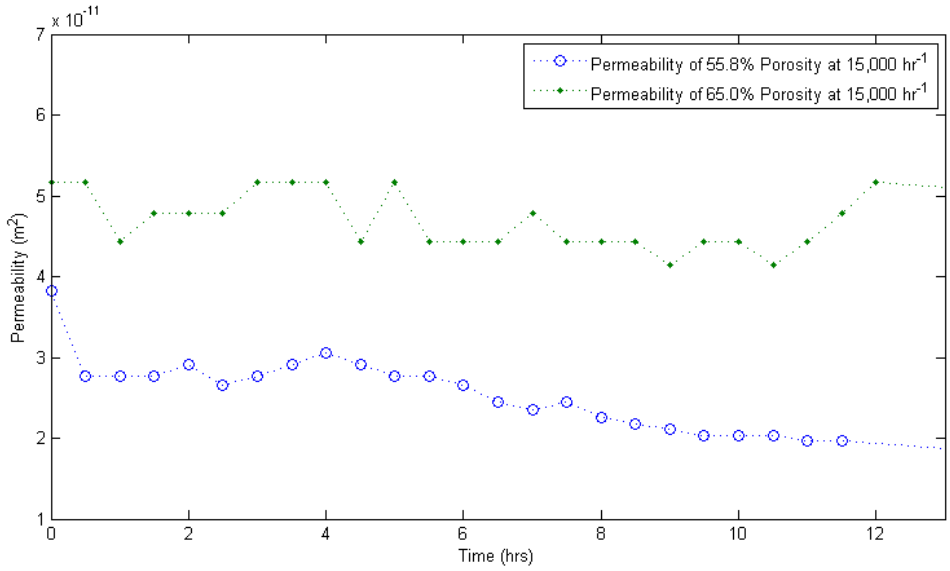

Figure 18 - Effect of porosity on permeability

4.1 Summary

Filtration efficiency increases with loading and decreasing flowrate and porosity, where CPSI of the filters is held constant. CPSI effects the filtration of filters by changing the surface velocity experienced by the filter wall. In the particle size range from 50nm to 350 nm, smaller particulate are more efficiently filtered. Permeability of filters decreases with increasing loading and flowrate, and can also be effected by the lower surface velocity caused by increased CPSI. The use of spherical salt particles instead of soot is an approximation made by many researchers that simplifies the modeling of the system, but may cause some differences from the filtration of actual particulate from engine exhaust. It's likely that aspherical particles would have higher filtration efficiency than spherical particle of the same mobility diameter. This is because for some orientations the aspherical particle is more likely to encounter a pore throat in the filter and be collected, while spherical particle could pass more easily through the filter wall. Then it may

be that the filtration efficiencies presented here are underestimations of what would be seen in the filtration of actual exhaust emissions.

5 MODEL DEVELOPMENT

In this work, the Opris and Johnson model [31] was modified to more accurately describe the filtration behavior of filter samples without a soot cake by the removal of cake-filtration related approximations. Additional modes of sedimentation and thermophoretic were incorporated, to supplement the Brownian diffusion, inertial impaction, and direct interception modes already accounted in the Opris model.

5.1 Brownian Diffusion

Filtration by Brownian diffusion occurs when particulate entrained in a flow of fluid deviate from their flowpath due to Brownian motion, and are thus intercepted by a grain of the filter. Filtration by this mode increases with temperature and decreases with increasing flowrate or particle diameter. The equations governing Brownian diffusion are given below.

$$E_D = 2.86\left(1 + 0.388 \cdot Kn \cdot \left(\frac{Pe}{Y}\right)^{\frac{1}{3}}\left(\frac{Pe^{\frac{2}{3}}}{Y^{\frac{1}{3}}}\right)\right) \quad (1)$$

$$Y = H + 1.966 \cdot Kn\left(H + 0.05\right) \quad (2)$$

$$H = 0.75 - 0.5\log\beta \quad (3)$$

$$\beta = 1 - \varepsilon \quad (4)$$

$$\lambda = \frac{\mu}{0.499 \cdot P\sqrt{\frac{8000}{\pi \cdot R \cdot T_i}}} \quad (5)$$

5.2 Inertial Impaction

Inertial impaction may occur when an entrained particle's flowpath curves due to the cell structure of the filter. Larger particles may be ejected from the flow by their greater momentum,

and thereby intercept a grain of the filter. Filtration by impaction thus increases with increasing particle diameter or flowrate. This filtration mode is affected by the Stokes number, *Stk*, and by the ratio of diameter of the particle, d_p, to the pore diameter, p_d. The equations describing inertial impaction are given below.

$$E_I = 0.16 \cdot N_R + \left(0.5 + 0.8 \cdot N_R\right) Stk - 0.105 \cdot Stk^2 \quad (6)$$

$$N_R = \frac{d_p}{p_d} \quad (7)$$

$$Stk = \frac{\left(\rho_p - \rho_g\right) \cdot {d_p}^2 \cdot u}{18 \cdot \mu \cdot p_d} \quad (8)$$

5.3 Direct Interception

Filtration by direct interception occurs when a grain of the filter is directly in the path of an entrained particle. The particle intercepts the grain and collects on the surface of it. Equations describing direct interception are given below..

$$E_R = \frac{N_R\left(N_R + 1.996 \cdot Kn\right)}{\tilde{H} + 1.996 \cdot Kn\left(\tilde{H} + 0.5\right)} \quad (9)$$

$$\tilde{H} = 2 - \log(\mathrm{Re}) \quad (10)$$

5.4 Sedimentation

Sedimentation is caused by gravity's effect on particulate. Larger, more massive particles may lose entrainment and be collected by the filter. The density of the particle is ρ_p and the density of the gas is ρ_g.

$$E_G = \frac{\rho_p - \rho_g}{(18 \cdot \mu \cdot u) \cdot 9.81 \cdot {d_p}^2} \tag{11}$$

5.5 Thermophoresis

Filtration due to thermophoresis occurs at the channel level, rather than in the porous walls of the filter bed. Particulate will be caused to move by a temperature gradient. This effect increases with the thermal conductivity of the particle, with the steepness of the gradient, and decreases with flowrate. The Prandtl number is given by *Pr*, and the Nusselt number by *Nu.*

$$E_T = \frac{C_c \cdot \rho_g \cdot c_p \cdot \mathrm{Re}_{De} \cdot f \cdot K_{th} \cdot \nu \cdot (T_i - T_w)}{De \cdot h \cdot \bar{T} \left(1 - e^{\left(\frac{-C_a \cdot P \cdot h \cdot L}{\rho_g \cdot Q \cdot c_p}\right)}\right)} \tag{12}$$

$$\bar{T} = \frac{T_i + T_w}{2} \tag{13}$$

$$h = \frac{k_g \cdot Nu_{De}}{De} \tag{14}$$

$$Nu_{De} = \frac{f \cdot (\mathrm{Re}_{De} - 1000) \cdot \mathrm{Pr}}{8 \cdot \left(1 + 12.7\sqrt{\frac{f}{8}}\left(\mathrm{Pr}^{\frac{2}{3}} - 1\right)\right)} \tag{15}$$

$$K_{th} = \frac{2.294\left(\frac{k_g}{k_p} + 2.2 \cdot Kn\right) \cdot Cu}{(1 + 3.438 \cdot Kn)\left(1 + \frac{2k_g}{k_p} + 4.4 \cdot Kn\right)} \tag{16}$$

$$Cu = 1 + \left(\frac{2 \cdot \lambda}{d_p}\right) \cdot \left(1.257 + 0.4e^{\left(\frac{-0.55 \cdot d_p}{\lambda}\right)}\right) \tag{17}$$

$$f = 0.3164 \cdot \left(\mathrm{Re}_{De}\right)^{-.25} \tag{18}$$

$$D = \frac{B \cdot T_i}{3 \cdot \pi \cdot \mu \cdot d_p} \tag{19}$$

5.6 Overall Filtration

The overall filtration efficiency is calculated as shown below. E_D, E_R, E_I, E_G, and E_T are the specific efficiencies due to Brownian diffusion, direct interception, inertial impaction, sedimentation, and thermophoresis respectively. One empirical fitting factor, was used to tune the model to experimental data, shown in equation (21) as '*C'*.

$$\eta = 1 - e^{-\alpha} \tag{20}$$

$$\alpha = \left(\frac{4\beta w}{\pi \varepsilon d_p}\right)\left(C \cdot E_D + E_R + E_I\right) + \frac{-3\beta}{4\left(\frac{d_c}{2}\right)} E_G + E_T \tag{21}$$

The value of *C* was chosen by inspection for each average zero hour filtration efficiency distribution for three porosities each at two flowrates. Specifically, the values were chosen to minimize the difference between model and experiment in the region from 50 to 100 nm, which is the size range for GDI particulate emissions. The value of *C* was changed incrementally until the model trend, for example the one shown in Figure 19, transitioned from underestimation to overestimation of experiment, thereby giving bounds on *C*. This was repeated with smaller increments until an optimum value was achieved to two decimal places. This iterative method was used due to the ease with which *C* can be varied and the model predictions replotted for inspection rather than the more difficult option of attempting to predict how much the model would change for a given change in *C*.

5.7 Comparison and Validation of Models

Figure 19 compares experimental data at 15,000 hr^{-1} to simulated filtration efficiency for the Opris model and the modified model. The increase in modeled filtration efficiency in the Opris model is due to the presence of soot cake approximations. Removing these yields a model that is in good agreement with experimental data. Figure 20 shows the absolute value of the difference between experimental and modeled data. For 15,000 hr^{-1}, this difference never exceeds 6% efficiency. If we consider only the range from 50nm to 100nm, which is the size range of GDI particulate, then the error is smaller; less than 1% efficiency. Figure 19 through Figure 22 shows the results of a particle size range from 25nm, the smallest the SPMS can count, to 350nm. However, our primary concern is for the range of GDI sized particulate. For all porosities in both Figure 19 and Figure 21, the model's slope is different from that of experimental data in the range from about 25nm to 40 nm. It's possible that the particulate counts should be treated with some caution as the instrument approaches the lowest extreme of particle size that the SMPS can measure, as the instrument may begin to count fewer particles than exist. However, since the GDI particle size range lies between 50nm and 100nm, this disparity does not prevent us from drawing conclusion about filtration efficiency in the range of interest.

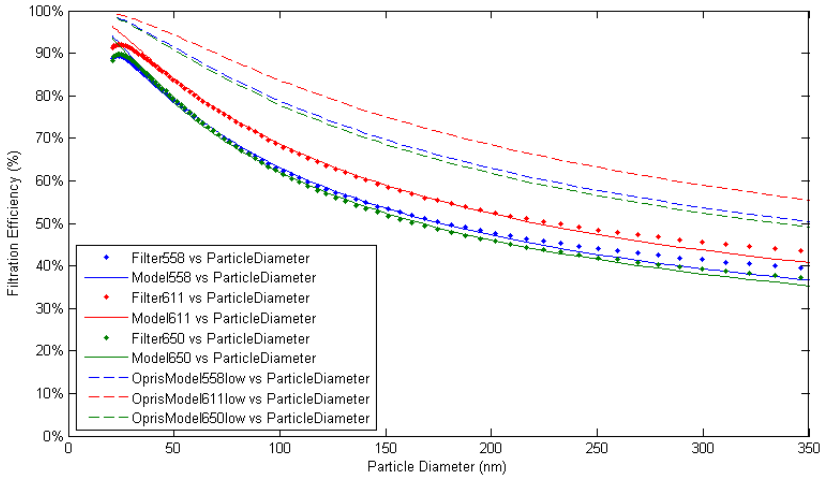

Figure 19 - Model validation and model comparison at 15,000 hr -1

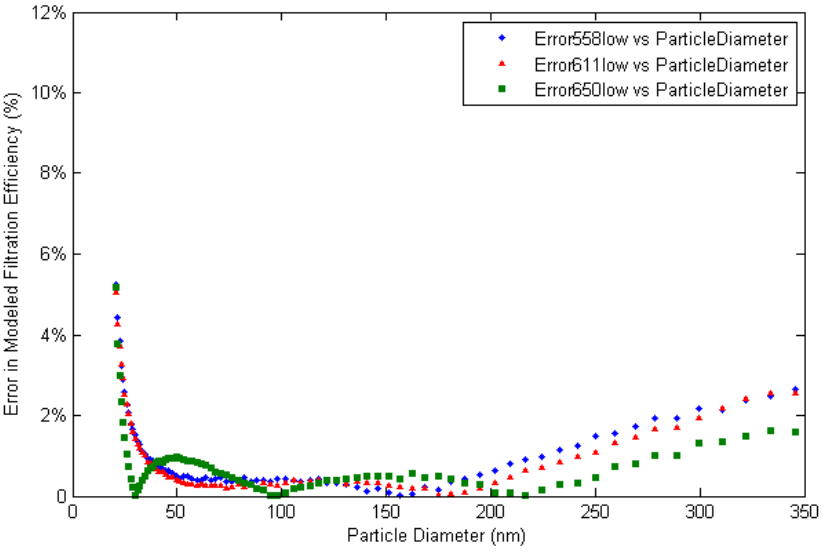

Figure 20 - Error of modeled filtration efficiency at 15,000 hr -1. This plot displays the absolute value of the subtraction of modeled and experimental filtration efficiency, in percent.

Figure 21 shows the agreement between modeled filtration efficiency and experimental filtration efficiency at 30,000 hr^{-1}. Also shown are the filtration efficiencies simulated by the Opris model, run with the same values of empirical fit factor. The current model represents an improvement over the previous model. Figure 22 shows the difference between the modeled and measured filtration efficiency at 30,000 hr^{-1}. This error is not greater than 2% efficiency in the particle size range of interest from 50nm to 100 nm.

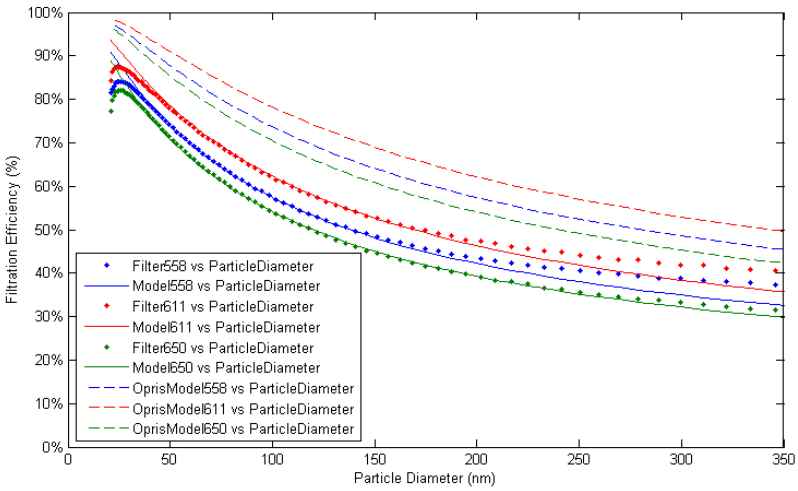

Figure 21 - Model validation and model comparison at 30,000 hr^{-1}

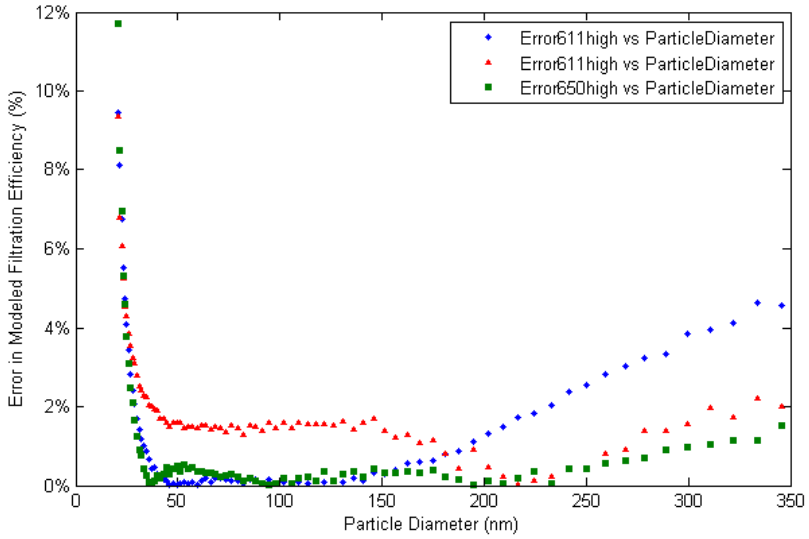

Figure 22 - Error of modeled filtration efficiency at 30,000 hr $^{-1}$ This plot displays the absolute value of the subtraction of modeled and experimental filtration efficiency, in percent.

The empirical fit factor *C* used to tune the average zero hour filtration efficiency distribution for three porosities each at two flowrates is given below in Figure 23. As before, the values for the 61.1% porous filter do not follow the trend, but all other values vary consistently with flowrate and porosity. It seems likely that this fit factor then represents either some missing portion of the model or, more likely, that some of the empirical coefficients in the previous models and fluid dynamics upon which this model is based may need reconsideration.

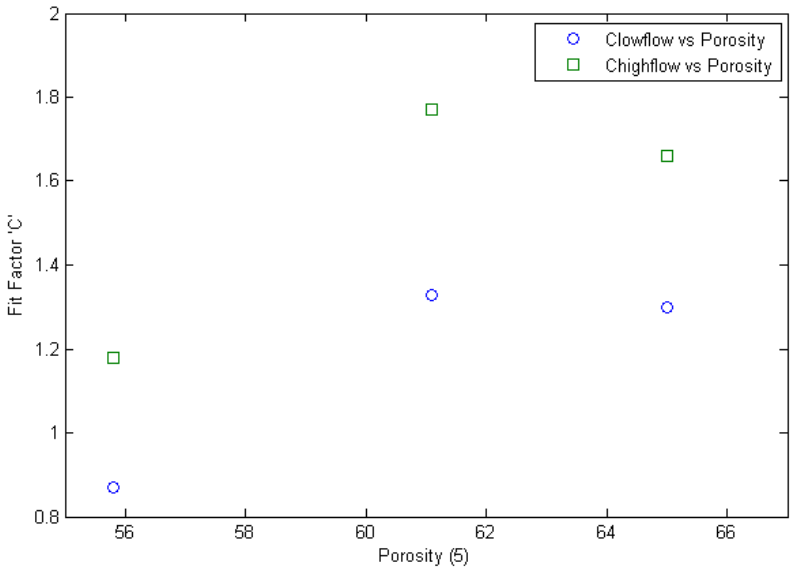

Figure 23 -Effect of Porosity and Flowrate on Experimental Fit Factor

6 SUMMARY

The purpose of this work was to study the size-dependent filtration efficiency of diesel particulate filters operating on particulate in the GDI size range, and to produce a model capable of predicting the filtration efficiency as a function of particle diameter and system parameters such as filter porosity, flowrate, and gas temperature. The model agrees well with experiment and does not deviate by more than 2% efficiency, and therefore represents an improvement over previous models. Filtration efficiency increases with loading and decreasing flowrate and porosity, where CPSI of the filters is held constant. CPSI effects the filtration of filters by changing the surface velocity experienced by the filter wall. In the particle size range from 50nm to 350 nm, smaller particulate are more efficiently filtered. Permeability of filters decreases with increasing loading and flowrate, and can also be effected by the lower surface velocity caused by increased CPSI.

6.1 Future Work

The study's purpose was to investigate the filtration of existing substrates (DPFs) under previously untested ranges or particle size. This work uses exclusively cordierite filters since this material is commonly used in DPFs, but it would be of interest to investigate additional filter substrates and materials that are in use filtering on-road engine technologies, such as silicon carbide and aluminum titanate. This work includes data from a trio of porosities with mis-matched cell geometries (CPSI). The conclusions reached here could be strengthened with more variety of porosity and CPSI to complete one or more sets of porosities with matched CPSI. Another topic of interest would be investigation into the effect of temperature on filtration efficiency, since all the tests included here were conducted at room temperature. Finally, the physical nature of C is still left to be determined. As shown in Figure 23, the fit factor varies consistently with flowrate, regardless of porosity. Since the model is based on both fluid

dynamics and previous filtration models that often have empirical fits built into them, it is possible that one or more of these is affecting the modeling efforts. Ideally, by understanding the effect of system parameters on the fit factor, it could be removed entirely.

NOMENCLATURE

α	Filtration exponential factor
β	Portion of the filter which is substrate
ε	porosity
λ	Mean free path
η	Filtration efficiency
μ	Dynamic viscosity
B	Boltzman's constant
Cu	Cunningham factor
d_p	Diameter of filter pores
p_d	Particle diameter
Pe	Peclet number
Pr	Prandtl number
Kn	Knudson number
Re	Reynolds number
AIM	Aerosol Instrument Manager
CPC	Condensation Particle Counter
CPSI	Cells per Square Inch
DMA	Differential Mobility Analyzer
DPF	Diesel Particulate Filter
GDI	Gasoline Direct Injection
MFC	Mass Flow Controller
PNNL	Pacific Northwest National Laboratory
US-EPA	United States Environmental Protection Agency

SMPS	Scanning Mobility Particle Sizer
WHO	World Health Organization

REFERENCES

1. Attfield, M., et al., The Diesel Exhaust in Miners Study: A Cohort Mortality Study With Emphasis on Lung Cancer. JNCI, 2012. 104(11): p. 869-883.

2. Maricq, M. How are emissions of nuclei mode particles affected by new PM control technologies and fuels? in HEI Annual Conference. 2009.

3. Mathis, U., M. Mohr, and R. Zenobi, Effect of organic compounds on nanoparticle formation in diluted diesel exhaust. Atmospheric Chemistry and Physics Discussions, 2004. 4: p. 227-265.

4. Heyder, J., Deposition of inhaled particles in the human respiratory tract and consequences for regional targeting in respiratory drug delivery. Proceedings of the American Thoracic Society, 2004. 1(4): p. 315-20.

5. Donaldson, K., Nanoparticles and the cardiovascular system: a critical review. Nanomedicine, 2013. 8(3): p. 403.

6. Bissett, E. and F. Shadman, Thermal Regeneration of Diesel-Particulate Monolithic Filters. AIChE Journal, 1985. 31(5): p. 753-758.

7. Merkel, G., et al., Effects of microstructure and cell geometry on performance of cordierite diesel particulate filters. SAE technical paper series, 2001. 2001-01-0193.

8. Opris, C. Catalyzed Diesel Particulate Trap: Technology Assessment. in US. DOE Diesel Engine Emissions Reduction (DEER) Conference. 2001. Portsmouth, VA.

9. Technical basis for retrofitting big vehicle fleets, F.a.L. Swiss Agency for the Environment, Editor 2002.

10. Pattas, K., et al., Comparative assessment of DPFs of different materials: A case study on a euro i light duty truck. SAE technical paper series, 2001. 2001-01-1287.

11. Hashimoto, S., et al., SiC and cordierite diesel particulate filters designed for low pressure drop and catalyzed, uncatalyzed systems. SAE technical paper series, 2002. 2002-01-0322.

12. Merkel, G., et al. New Cordierite Diesel Particulate Filters for Catalyzed and Non-Ca Applications. in US Department of Energy Diesel Engine Emission Reduction (DEER) Conference. 2003. Newport.

13. Pace, L., R. Pace, and M. Konieczny, Metal supported particulate matter-cat, a low impact and cost effective solution for a 1.3 euro IV diesel engine. SAE technical paper series, 2005. 2005-01-0471.

14. Ogyu, K., et al., Study on filter substrate structure for lower backpressure and higher regeneration performance. SAE technical paper series, 2006. 2006-01-1526.

15. Iwasaki, S., et al., New Design Concept for Diesel Particulate Filter. SAE international journal of engines, 2011. 2011-01-0603(1): p. 527-536.

16. Ogunwumi, S., et al., Aluminum titanate compositions for diesel particulate filters. SAE technical paper series, 2005. 2005-01-0583.

17. Heibel, A., et al. Performance and Durability of the New Corning DuraTrap® AT Diesel Particulate Filter – Performance and Durability Evaluation Results from Engine Bench and Vehicle Tests. in Aachen Kolloquium. 2005. Aachen.

18. Kercher, L. in Dresden Conference "Emission Control 2006". 2006. Technical University – Dresden.

19. Boger, T., et al., Next generation aluminum titanate filter for light duty diesel applications. 2011.

20. Ogyu, K., et al., Characterization of thin wall SIC-DPF. SAE technical paper series, 2003. 2003-01-0377.

21. Mizutani, T., et al., The study for structural design of the segmented SiC-DPF. SAE technical paper series, 2006. 2006-01-1527.

22. Mao, F. and C. Mao, Performance validation of an advanced diesel particulate filter with high catalyst loading capacity. SAE technical paper series, 2005. 2005-01-3696.

23. Kassel, R., et al., Ultrafine Particulate Matter and the Benefits of Reducing Particle Numbers in the United States, 2013, Manufacturers of Emission Controls Association (MECA).

24. Cookson, J., Removal of submicron particles in packed beds. Environmental science & technology, 1970. 4(2): p. 128-134.

25. Payatakes, A., A New Model for Granular Packed Media. AIChE Journal, 1973. 19(1).

26. Kuwabara, S., The forces experienced by a lattice of elliptic cylinders in a uniform flow at small reynolds numbers. Journal Of The Physical Society Of Japan, 1959. 14(4): p. 522-527.

27. Lee, K. and J. Lee, Collection of aerosol particles by packed beds. Environmental science & technology, 1979. 13(4): p. 466-470.

28. Pandse, H. and C. Tien, A Simulation Model of Aerosol Collection in Granular Media. Journal of Colloid and Interface Science, 1981. 87(1): p. 225-241.

29. Bissett, E., Mathematical model of the thermal regeneration of a wall-flow monolith diesel particulate filter. Chemical Engineering Science, 1984. 39(7-8): p. 1233-1244.

30. Konstandopoulos, A. and J. Johnson, Wall-Flow Diesel Particulate Filters—Their Pressure Drop and Collection Efficiency, 1989, SAE International.

31. Opris, C. and J. Johnson, A 2-D Computational Model Describing the Flow and Filtration Characteristics of a Ceramic Diesel Particulate Trap. SAE Technical Papers, 1998. 980545.

32. Pontikakis, G., G. Koltsakis, and A. Stamatelos, Dynamic filtration modeling in foam filters for diesel exhaust. Chemical engineering communications, 2001. 188: p. 21-46.

33. Liu, Z. and R. Miller, Flow Distributions and Pressure Drops of Wall-Flow Diesel Particulate Filters. papers.sae.org, 2002.

34. Huynh, C., et al., A one-dimensional computational model for studying the filtration and regeneration characteristics of a catalyzed wall-flow diesel particulate filter. SAE transactions, 2003. 2003-01-0841(4): p. 620-646.

35. Marre, S., et al., Modeling of submicrometer aerosol penetration through sintered granular membrane filters. Journal of colloid and interface science, 2004. 274(1): p. 167-182.

36. Sbrizzai, F., P. Sbrizzai, and A. Faraldi, Appraisal of three-dimensional numerical simulation for sub-micron particle deposition in a micro-porous ceramic filter. Chemical engineering science, 2005. 60(23): p. 6551-6563.

37. Ohara, E., et al., Filtration Behavior of Diesel Particulate Filters (1). SAE Technical Paper, 2007. 2007-01-0921.

38. Liu, Y., et al., Nanoparticle motion trajectories and deposition in an inlet channel of wall-flow diesel particulate filter. Journal of aerosol science, 2009. 40(4): p. 307-323.

39. Bensaid, S., et al., Modelling of diesel particulate filtration in wall-flow traps. Chemical engineering journal, 2009. 154(1): p. 211-218.

40. Tandon, P., et al., Measurement and prediction of filtration efficiency evolution of soot loaded diesel particulate filters. Chemical Engineering Science, 2010.

41. Wang, X., et al., Particle deposition on the wall driven by turbulence, thermophoresis and particle agglomeration in channel flow. Proceedings of the Combustion Institute, 2011. 33(2): p. 2821-2828.

42. Yang, J., et al., Single wall diesel particulate filter (DPF) filtration efficiency studies using laboratory generated particles. Chemical Engineering Science, 2009. 64: p. 1625-1634.

43. Zelenyuk, A. and D. Zelenyuk, On the Effect of Particle Alignment in the DMA. Aerosol science and technology, 2007. 41(2): p. 112-124.

44. Vaden, T., et al., Extending the Capabilities of Single Particle Mass Spectrometry: I. Measurements of Aerosol Number Concentration, Size Distribution, and Asphericity. Aerosol Science and Technology, 2011. 45(1): p. 113-124.

45. TSI, Model 3076 Constant Output Atomizer - Operation and Service Manual. 2011.

46. TSI, Series 3080 Electrostatic Classifiers - Operation and Service Manual. 2011.

47. TSI, Model 3087 Aerosol Neutralizer - Operation and Service Manual. 2011.

48. TSI, Model 3787 General Purpose Water-based Condensation Particle Counter - Operation and Service Manual. 2011.

APPENDIX

Additional Equations

$$\mathrm{Re} = \frac{\rho_g \cdot u \cdot p_d}{\mu} \tag{22}$$

$$\mathrm{Pr} = \frac{c_p \cdot \mu}{k_g} \tag{23}$$

$$Kn = \frac{2 \cdot \lambda}{w} \tag{24}$$

$$Pe = \frac{u \cdot p_d}{D} \tag{25}$$

$$Q = \frac{-\kappa A}{\mu} \frac{\Delta p}{L} \tag{26}$$

Additional Figures

Characterization of Effect of Salt Distribution of Particle Size Distribution

To characterize the effect of salt solution concentration on particle size distribution, we created three separate 1 M stock solutions for both sodium chloride and ammonium sulfate. These stock solutions were diluted to produce three replicate concentrations each of 0.01 M, 0.025 M, 0.05 M, 0.075 M, and 0.1 M for each salt type. Every replicate solution was tested until seven consecutive tests were in good agreement. These seven tests were then averaged, and compared to averages of the same concentration and salt type. A comparison was made of the distribution peak location for each average. The characterization results are shown below.

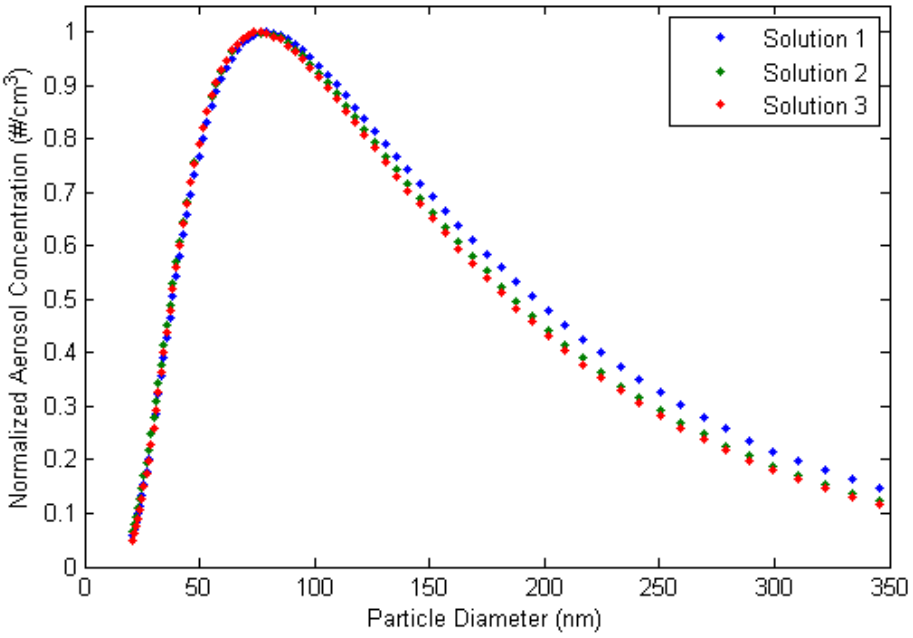

Figure 24 - Averages of 0.01 M ammonium sulfate iterations

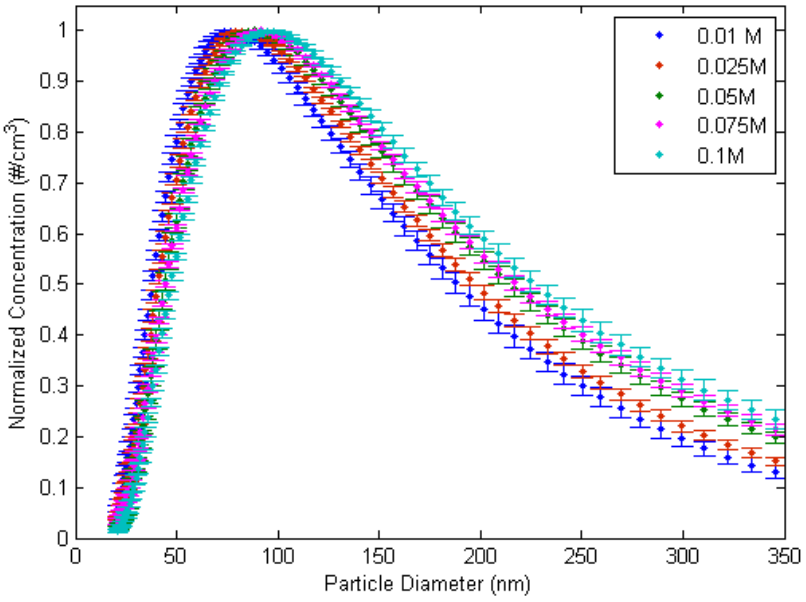

Figure 25 - Concentration effect on ammonium sulfate distribution

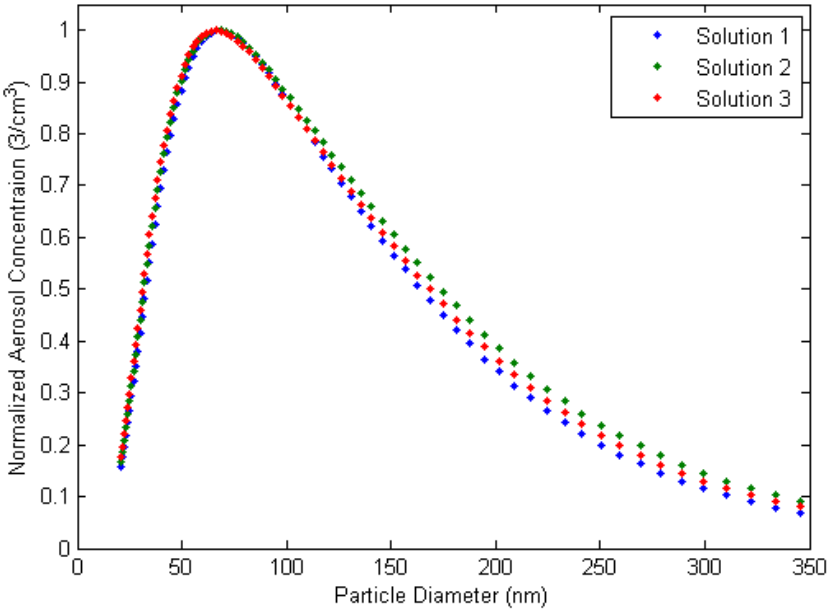

Figure 26- Average of 0.01 M sodium chloride iterations

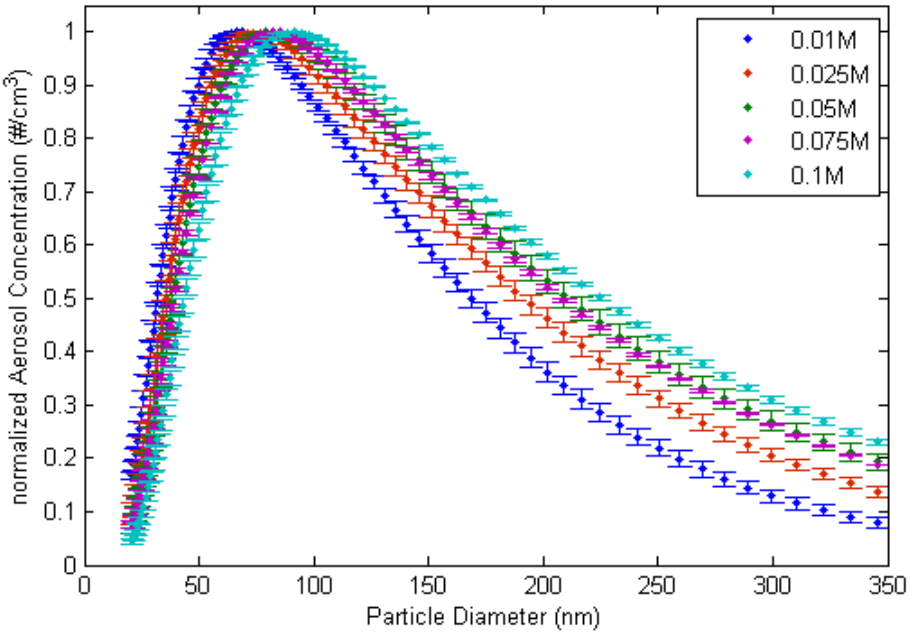

Figure 27- Concentration effect on sodium chloride distribution

Figure 24 and Figure 26 demonstrate the repeatability of the particle size distributions for 0.01 M concentrations of sodium chloride and ammonium sulfate, respectively, and are representative of the repeatability of every solution concentration. Figure 25 and Figure 27 demonstrate the effect of solution concentration on distribution peak location; peak location shifts to higher particle diameter as solution concentration increases. The distribution peak locations for all concentrations are plotted and fitted with an exponential function in Figure 28, and the values are listed in Table 1. The peaks of the ammonium sulfate distributions are located at larger particle diameter compared to those of sodium chloride solutions. The lack of deviation for the 0.01 M concentration of sodium chloride is an artifact of the fact that particle diameter is considered as discrete bins, and indicates that the deviation is smaller than the resolution of the DMA at that

diameter. For the experiments listed in following sections, we have chosen to use a 0.025 M concentration of ammonium sulfate.

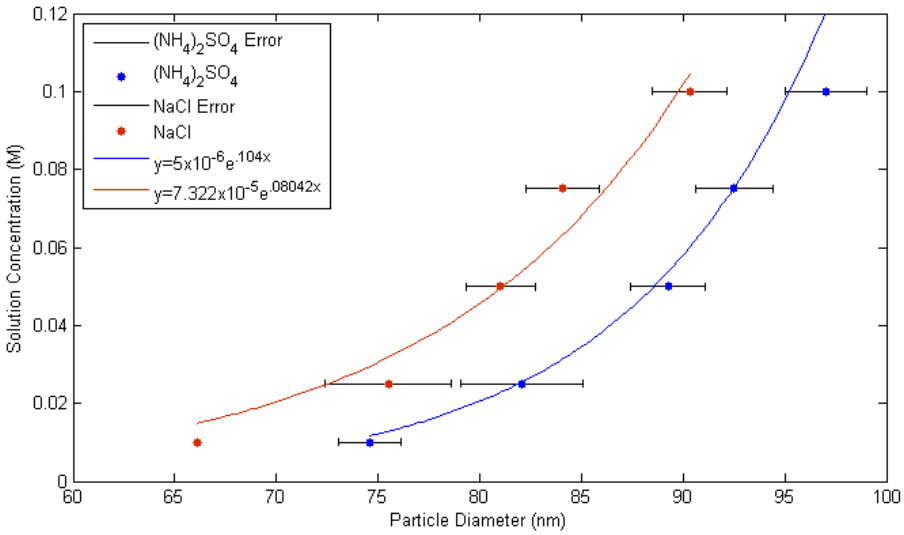

Figure 28 - Distribution peak location versus concentration

	$(NH_4)_2SO_4$		NaCl	
Concentration (M)	Average (nm)	Std. Deviation (nm)	Average (nm)	Std. Deviation (nm)
0.01	75	2	66	0
0.025	82	3	76	3
0.05	89	2	81	2
0.075	93	2	84	2
0.1	97	2	90	2

Table 1 - Averages and standard deviations of distribution peak locations

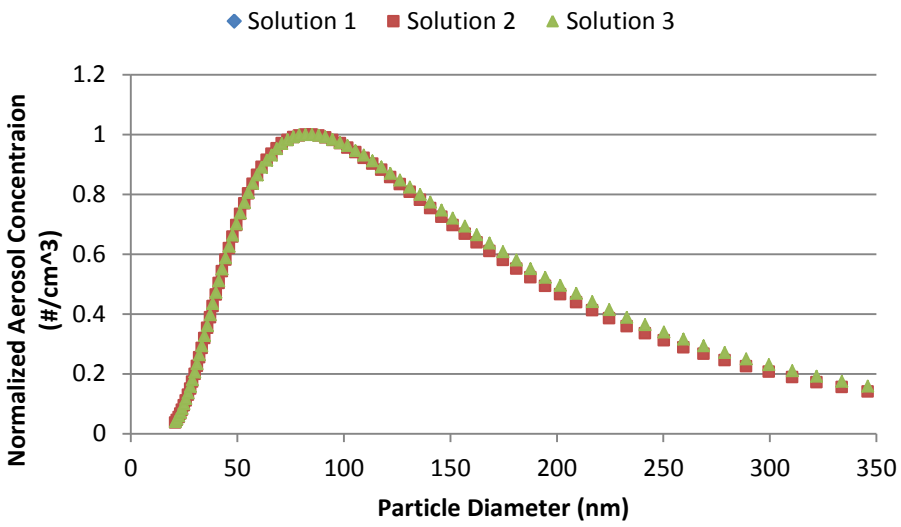

Figure 29 - Averages of 0.025 M ammonium sulfate iterations

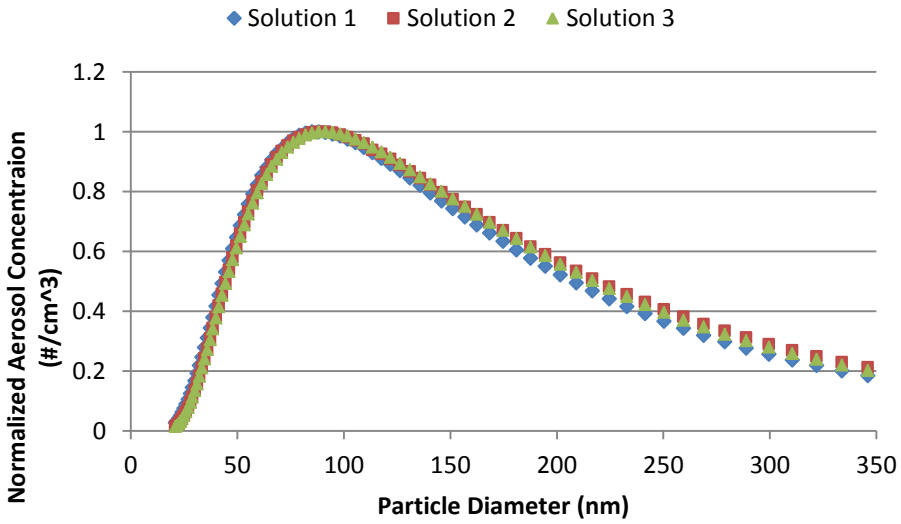

Figure 30 - Averages of 0.05 M ammonium sulfate iterations

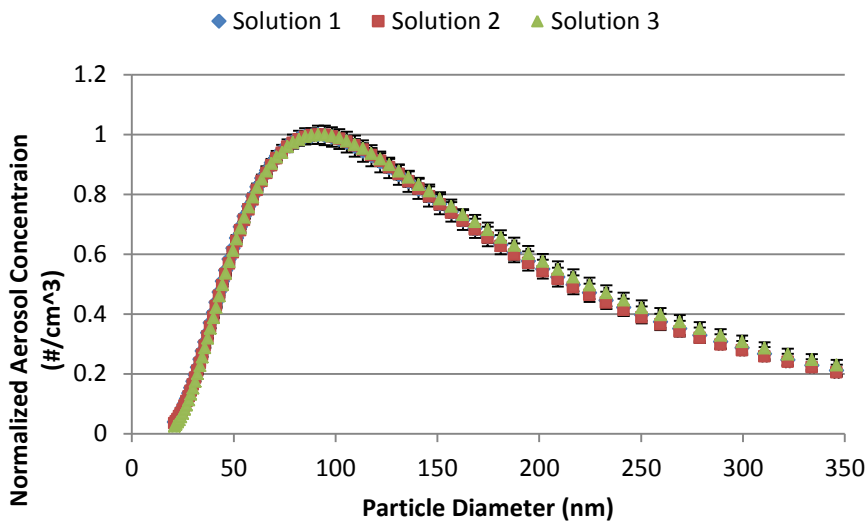

Figure 31 - Averages of 0.075 M ammonium sulfate iterations

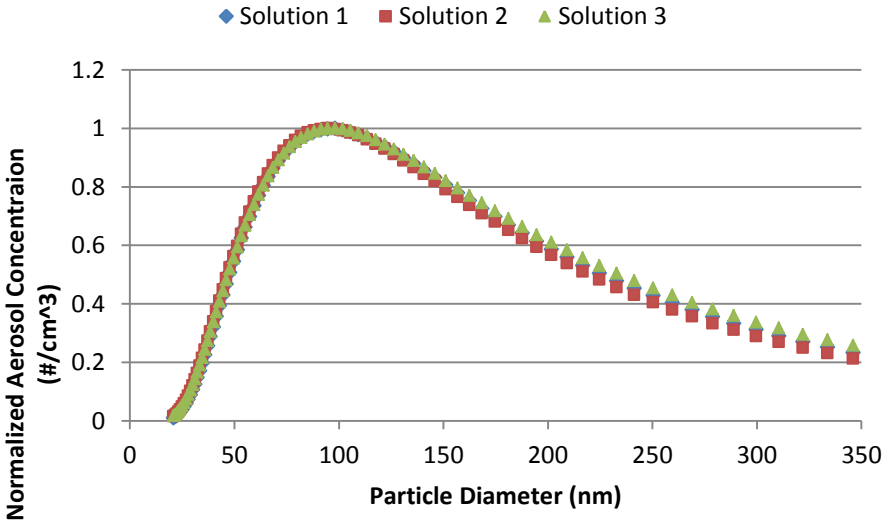

Figure 32 - Averages of 0.1 M ammonium sulfate iterations

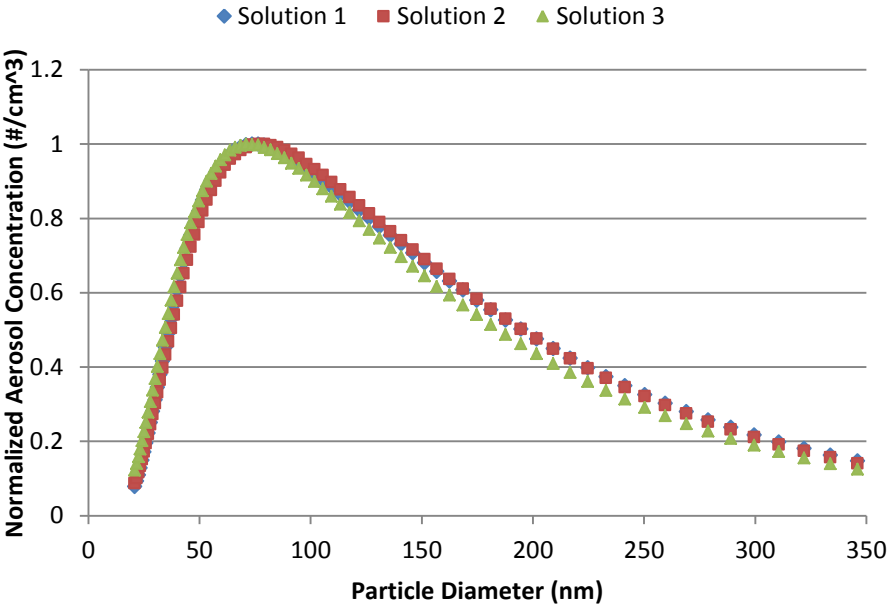

Figure 33 - Averages of 0.025 M sodium chloride iterations

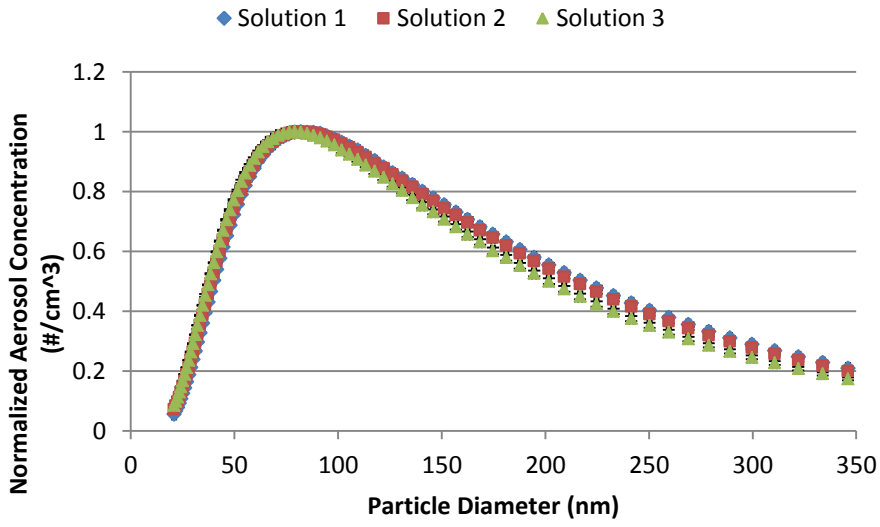

Figure 34 - Averages of 0.05 M sodium chloride iterations

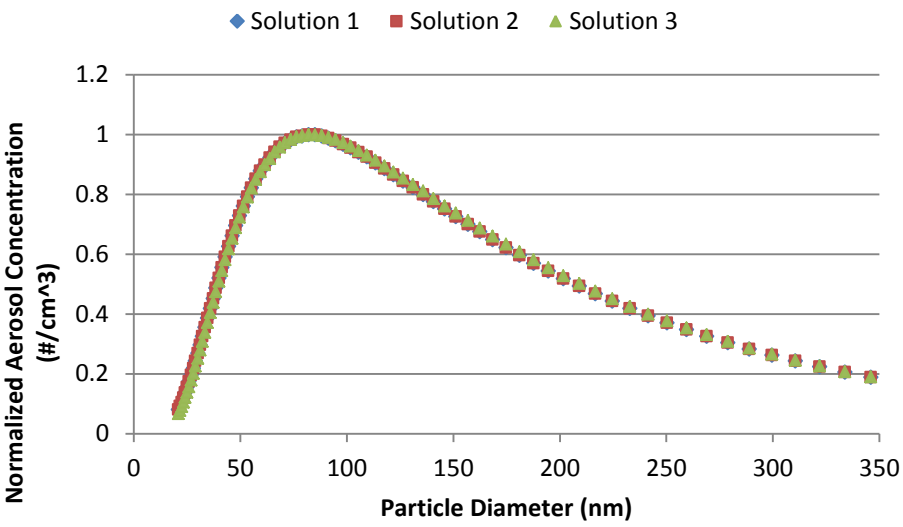

Figure 35 - Averages of 0.075 M sodium chloride iterations

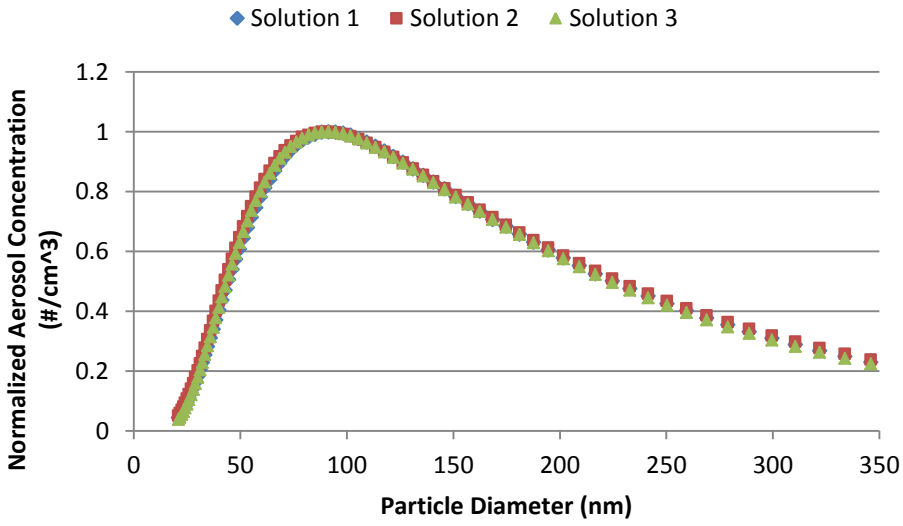

Figure 36 - Averages of 0.1 M sodium chloride iterations

System Losses Characterization

To measure the loss of particle counts caused by the sample holder while containing no filter sample, we tested the particle size distribution upstream and downstream of the empty sample holder. Seven replicates for each case were performed under the same conditions later used for filtration tests; employing 0.025 M ammonium sulfate to produce the aerosol, at both 15,000 hr^{-1} and 30,000 hr^{-1}. The averages of these replicates, and their standard deviations, are plotted in Figure 37 and Figure 38.

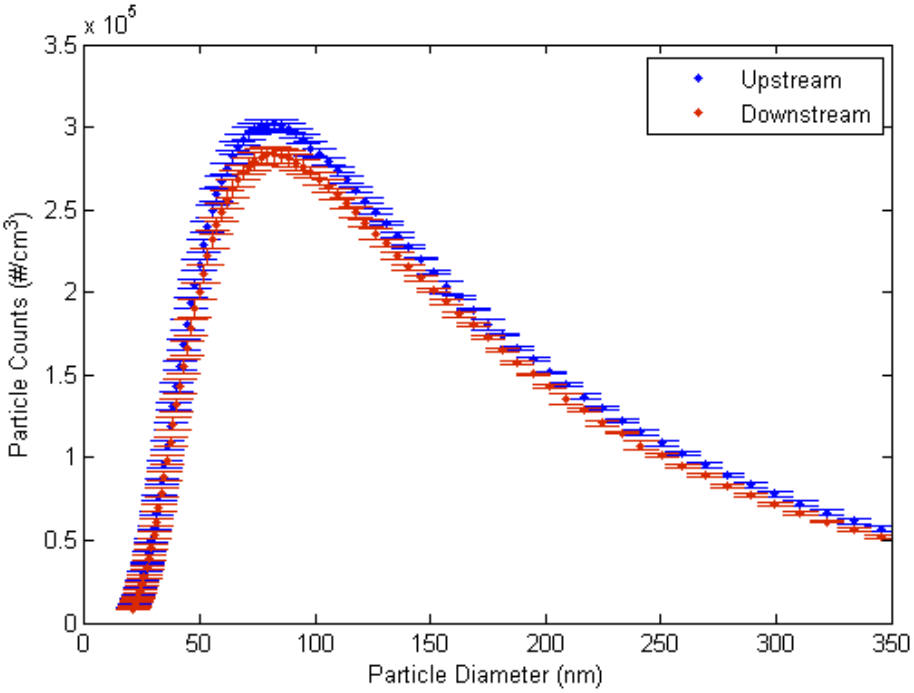

Figure 37 - Particle losses at 15,000 hr^{-1}

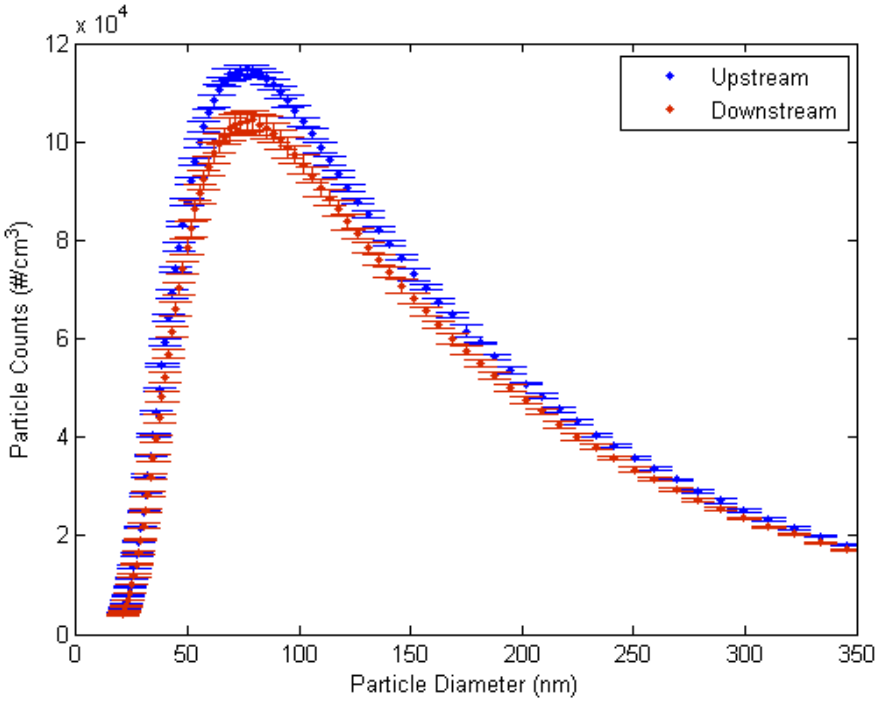

Figure 38 - Particle losses at 30,000 hr^{-1}

The standard error of each set of replicates was less than about 2% in the particle diameter range of 50nm to 150nm, and higher in some places outside this range due to low overall particle counts. Comparing the upstream and downstream particle number concentrations yields the system losses. The results of the system losses characterization are shown below in Figure 39.

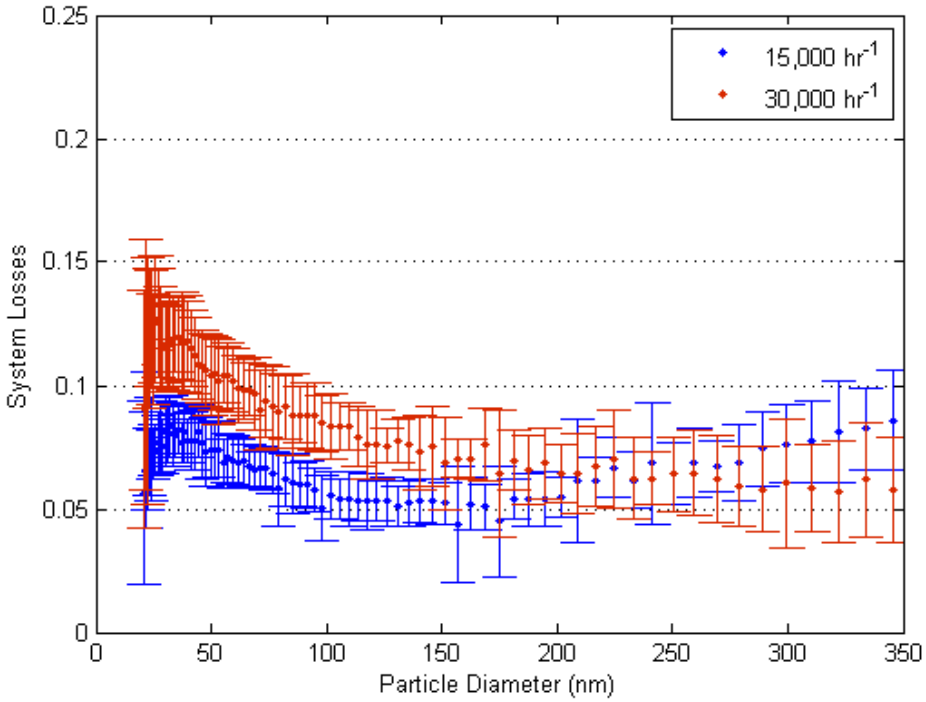

Figure 39 - System losses of sample holder while empty

Overall, the system losses at the higher flow rate were greater than at the lower flow rate, with the exception of particles above 250nm diameter. This may be due to greater effect at the lower flow rate of sedimentation due to gravity on particles that are larger and therefore heavier. Since the system losses are less than 10% in the 50nm to 150nm particle diameter range of interest, we may safely neglect them

Dilution Characterization

The experimental system includes an MFC that increases the flow rate provided to the filter by adding make-up air to the sample stream. This addition dilutes the particle concentration of the stream. To characterize the effect of dilution on particle number concentration, experiments were

conducted from 0ccm of make-up air to 18,500ccm, with flow rate step size of 500ccm. To convert the flow rate of the MFC in ccm to hr^{-1}, a Gilibrator bubble flow meter was employed to measure the flow rate exiting the constant output atomizer and exiting the MFC. These flows were summed and divided by volume of the filter sample to yield the correct unit. A representative plot of the dilution effect is given in Figure 40while the complete data set is given below.

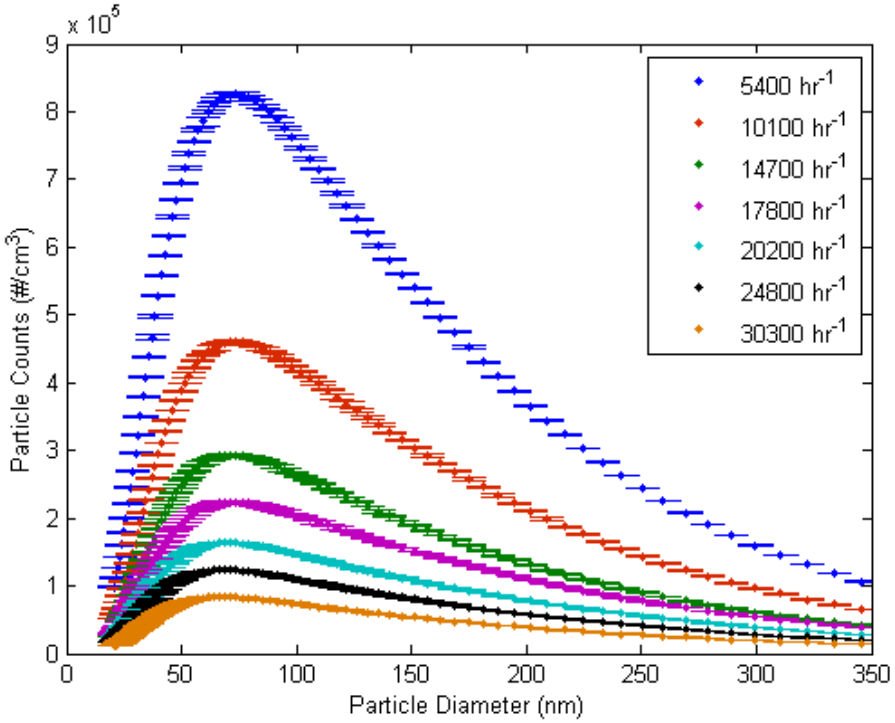

Figure 40 - Representative effect of dilution air on particle counts

For the majority of the filtration experiments listed below, we selected a flow rate of 15,000 hr^{-1}, because this yielded particle counts of not less than 100,000 in the particle diameter range from

50nm to 150nm. To test the effect of flow rate on filtration we also conducted filtration experiments on the 55.8% porosity samples at 30,000 hr^{-1} for comparison.

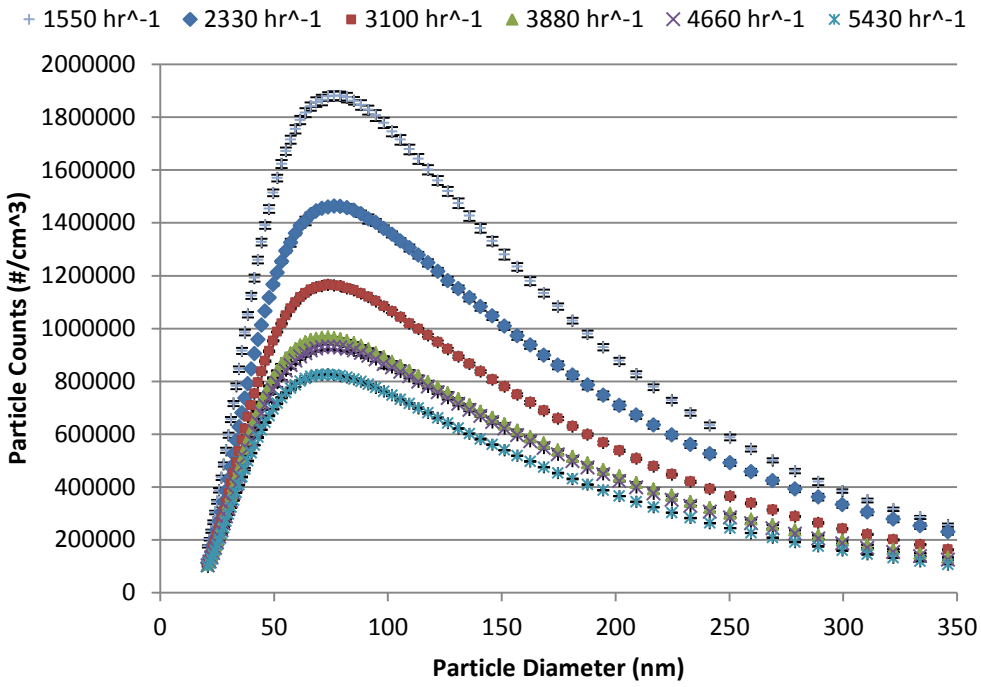

Figure 41 - Effect of dilution air on particle counts (1)

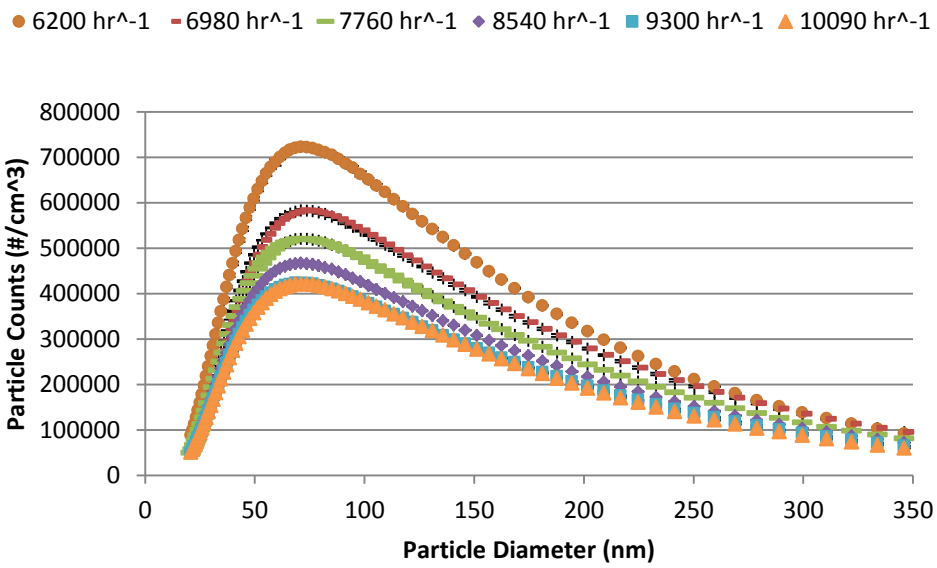

Figure 42 - Effect of dilution air on particle counts (2)

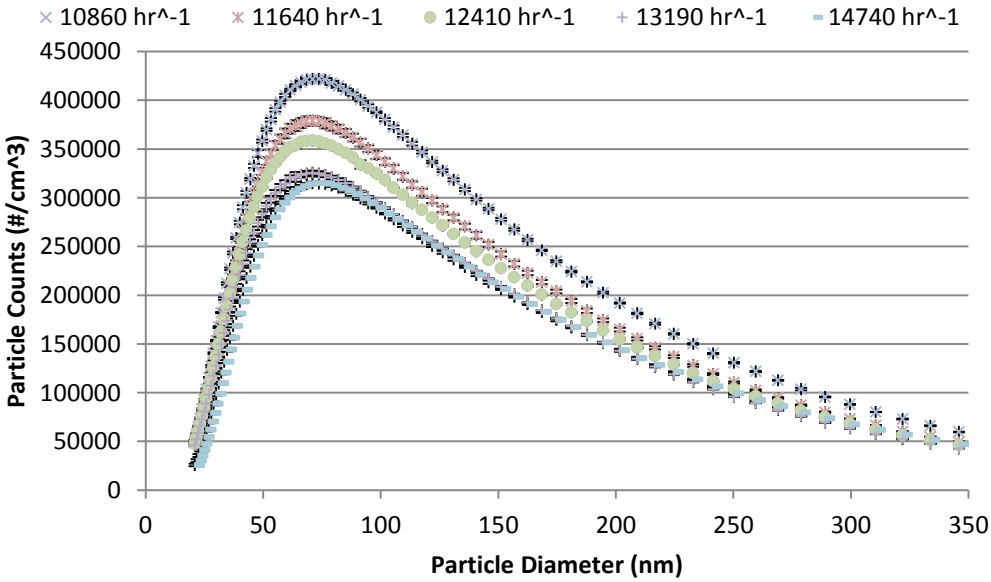

Figure 43 - Effect of dilution air on particle counts (3)

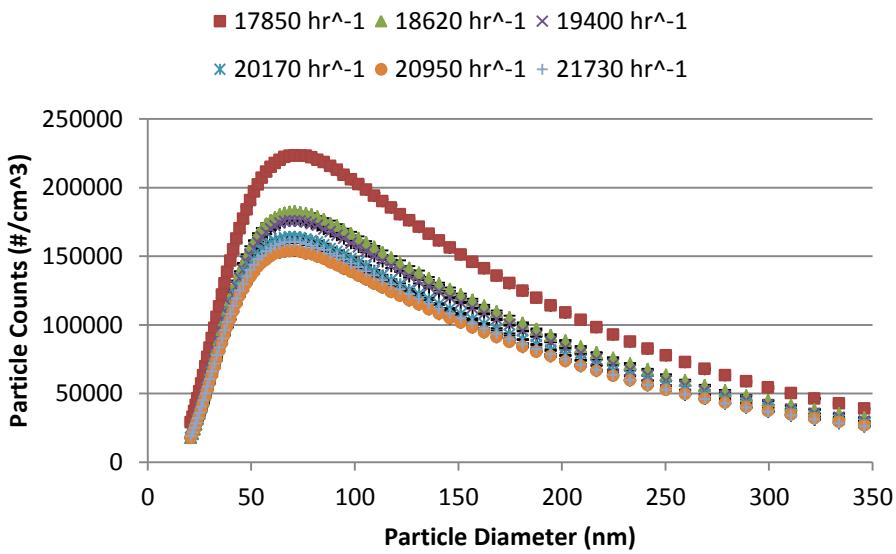

Figure 44 - Effect of dilution air on particle counts (4)

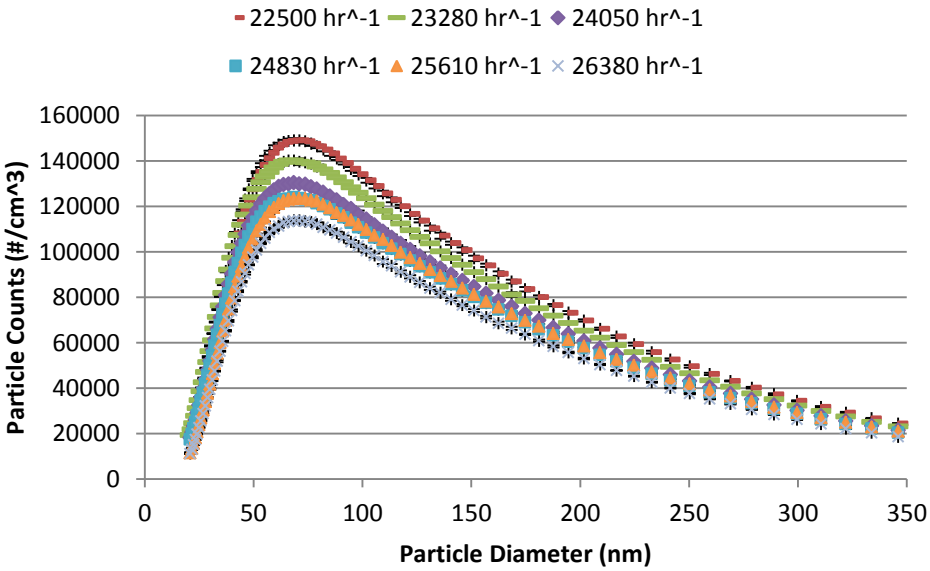

Figure 45 - Effect of dilution air on particle counts (5)

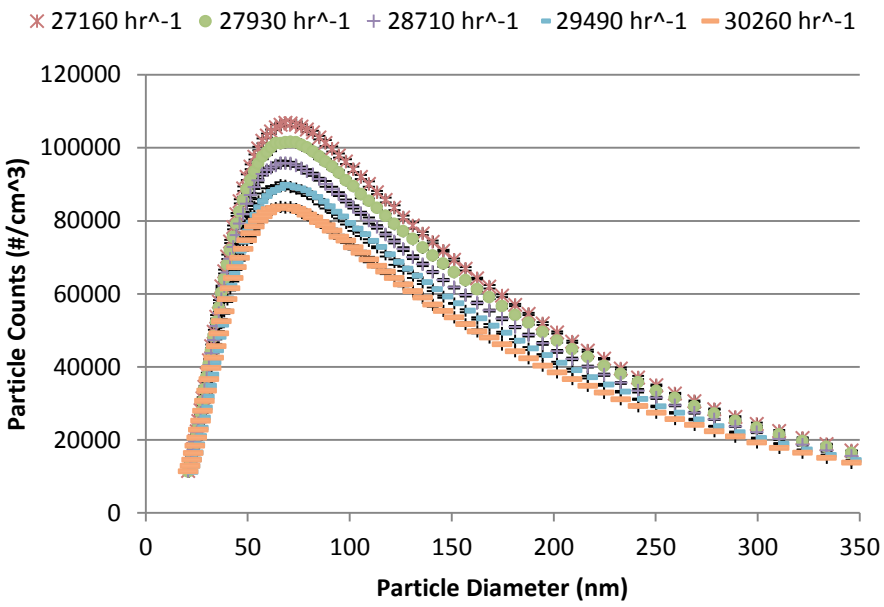

Figure 46 - Effect of dilution air on particle counts (6)

MATLAB programs

Simulation Model for Filters of 55.8% Porosity

```
function Output=ShepFilter558(Ti, Tw, Q)

%Q MUST be in m^3/sec
%the original thermophoresis programming expects Q to be m^3/hr,
so some
%conversions exists in those equations

epsilon=.558; %porosity
N=  61 ; %number of inlet channels, was 5765
AC1=1;  %arbitrary  constant  1     for  highflow,  use  AC1=1  and
AC2=1.18
AC2=.87;  %arbitrary  constant  2    for  lowflow  use  AC1=1  and
AC2=.87
w= .3 *10^-3; %WallThickness; %variable

CollectorDiameter=23.83;
```

```
ParticleDiameter=[20.9000000000000;21.7000000000000;22.5000000000000;...
    23.3000000000000;24.1000000000000;25;25.9000000000000;...

26.9000000000000;27.9000000000000;28.9000000000000;30;31.1000000000000;...

32.2000000000000;33.4000000000000;34.6000000000000;35.9000000000000;...

37.2000000000000;38.5000000000000;40;41.4000000000000;42.9000000000000;...

44.5000000000000;46.1000000000000;47.8000000000000;49.6000000000000;...

51.4000000000000;53.3000000000000;55.2000000000000;57.3000000000000;...

59.4000000000000;61.5000000000000;63.8000000000000;66.1000000000000;...

68.5000000000000;71;73.7000000000000;76.4000000000000;79.1000000000000;...

82;85.1000000000000;88.2000000000000;91.4000000000000;94.7000000000000;...

98.2000000000000;101.800000000000;105.500000000000;109.400000000000;...

113.400000000000;117.600000000000;121.900000000000;126.300000000000;...

131;135.800000000000;140.700000000000;145.900000000000;151.200000000000;...

156.800000000000;162.500000000000;168.500000000000;174.700000000000;...

181.100000000000;187.700000000000;194.600000000000;201.700000000000;...

209.100000000000;216.700000000000;224.700000000000;232.900000000000;...

241.400000000000;250.300000000000;259.500000000000;269;278.800000000000;...
```

```
289;299.600000000000;310.600000000000;322;333.800000000000;...
    346;358.700000000000;]*10^-9; %meters


%                                                ParticleDiameter
=[20.9000000000000;21.7000000000000;22.5000000000000;...
%     23.3000000000000;24.1000000000000;25;25.9000000000000;...
%     26.9000000000000;27.9000000000000;28.9000000000000;30;...
%     31.1000000000000;32.2000000000000;33.4000000000000;...
%     34.6000000000000;35.9000000000000;37.2000000000000;...
%     38.5000000000000;40;41.4000000000000;42.9000000000000;...
%     44.5000000000000;46.1000000000000;47.8000000000000;...
%     49.6000000000000;51.4000000000000;53.3000000000000;...
%     55.2000000000000;57.3000000000000;59.4000000000000;...
%     61.5000000000000;63.8000000000000;66.1000000000000;...
%     68.5000000000000;71;73.7000000000000;76.4000000000000;...
%     79.1000000000000;82;85.1000000000000;88.2000000000000;...
%     91.4000000000000;94.7000000000000;98.2000000000000;...
%
101.800000000000;105.500000000000;109.400000000000;113.400000000
000;...
%     117.600000000000;121.900000000000;126.300000000000;131;...
%
135.800000000000;140.700000000000;145.900000000000;151.200000000
000;...
%
156.800000000000;162.500000000000;168.500000000000;174.700000000
000;...
%
181.100000000000;187.700000000000;194.600000000000;201.700000000
000;...
%
209.100000000000;216.700000000000;224.700000000000;232.900000000
000;...
%     241.400000000000;250.300000000000;259.500000000000;269;...
%
278.800000000000;289;299.600000000000;310.600000000000;322;...
%     333.800000000000;346;358.700000000000;371.800000000000;...
%
385.400000000000;399.500000000000;414.200000000000;429.400000000
000;...
%
445.100000000000;461.400000000000;478.300000000000;495.800000000
000;...
%     514;532.800000000000;552.300000000000;572.500000000000;...
%
593.500000000000;615.300000000000;637.800000000000;661.200000000
000;...
```

```
%       685.400000000000;710.500000000000;736.500000000000;]*10^-
9; %meters
% ParticleDiameter=logspace(-2,1,300).*10^-6; %meters
%ParticlesIn=input(2,:);

PoreDiameter= 25*10^-6; %ceramic property D_f

ChannelLength= 225*10^-3;  %channelLength; %variable
ChannelWidth= 2*10^-3; % cellWidth; %variable
L=ChannelLength;
Ca= L/(4*ChannelWidth); %ratio of wall length of heat transfer
to the
%perimeter of the cross section
De=ChannelWidth; %=4*A/P Hydraulic Diameter
Peri= 4*ChannelWidth;

GasVelocity = Q/(N*4*ChannelWidth*L);

yvan=1; %van der Waals scale
Cc =0.82*(((ChannelWidth/2)./yvan).^(1/7));

Pressure=  6894.76*14.7/1000;  %abs  exhaust  gas  pressure,  kPa,
parameter

B=1.38*10^-23; %Boltsman's constant J/Kelvin
MW=29; %molar weight of the fluid
R_uni=8.314; %universal gas constant
R= R_uni/MW; %exhaust specific gas constant,

GasDensity=Pressure/(R*Ti);

MW=29; % molar weight of fluid
Pa_per_psi=6894.76;
PascalPressure=Pressure*Pa_per_psi;
rho=MW*PascalPressure/1000/(R_uni*Ti);

Cp=3*(10^-7)*(Ti-273).^2    +    5*(10^-5)*(Ti-273)    +    1.0029;
%specific heat of the gas
kg= 7*(10^-5)*(Ti-273) + 0.0245; %thermal conductivity of gas
%Cp and kg relationships are a regression of data given at
%engineeringtoolbox.com. Not valid past 400C

kp= 5.4*(300/Ti).^(1.14); %thermal conductivity of particle
%equation given in Clayton et al "Thermal-mechanical
%modeling  of  a  generic  high-level  waste  salt  repository"
Mechanical
%Behavior of Salt VII - Proceedings of the 7th Conference on the
Mechanical
%Behavior of Salt, 2012, pp.435-439
```

```
SuperficialVelocity = Q/(N*4*ChannelWidth*L); %written as v_wall
in the paper
ParticleVelocity=SuperficialVelocity; %approximately true

ParticleDensity=(2165); %kg/m^3
%this is for sodium chloride %will be a function of particle
diameter

mu=1.846*10^-5; %dynamic fluid viscosity
nu=mu/GasDensity;

Permeability= ((PoreDiameter.^2).*epsilon.^(5.5))/(5.6);

gamm=  sqrt((48.*Permeability.*L.^2)./(w.*ChannelWidth.^3));  %eq
12

PressureDrop=((6*mu*L*Q)./(N*ChannelWidth.^4))*...
    (2*(exp(gamm)+1)+gamm.*(exp(gamm)-1))./(gamm.*(exp(gamm)-
1));

ExpectedPressureDrop=mean(PressureDrop);

lambda    =    mu/(0.499.*Pressure.*((8/(pi*(R/1000)*Ti)).^0.5));
%mean free path

Kn = 2.*lambda./PoreDiameter; %knudson number

beta = 1-epsilon; %packing density

H = .75-.5*log(beta);

Y = H+1.996*Kn*(H+.05);

D = B.*Ti./(3*pi*mu.*ParticleDiameter); %Diffusion Coefficient

Pe = ParticleVelocity.*PoreDiameter./D; %pecklet number

Re_De = GasVelocity *ChannelWidth/ nu;  %reynolds number

f=0.3164*Re_De.^(-.25);

lambda    =    mu/(0.499.*Pressure.*((8/(pi*(R/1000)*Ti)).^0.5));
%mean free path

Kn  =  2.*lambda./ChannelWidth;  %knudson  number,  not  explicitly
defined by Wang
```

```
Cu=     1+     (2*lambda./ParticleDiameter).*(1.257     +.4.*exp(-
.55*ParticleDiameter./lambda));
%Cunningham correction factor, coefficients for air


Kth                                                                =
(2.294.*((kg/kp)+2.2*Kn)*Cu)/((1+3.438*Kn)*(1+2*(kg/kp)+4.4*Kn))
;

Pr= 10^-09*(Ti-273).^3 - 3*10^-07*(Ti-273).^2 - 0.0001*(Ti-273)
+ 0.7174; %Prandtl Number
%generally Pr=Cp.*mu./(kg), but this gives the temperature
dependence. This
%relationship is a regression of data given at
engineeringtoolbox.com.

Nu_De=((f/8)*(Re_De-1000)*Pr)/(1+12.7*sqrt(f/8)*((Pr.^(2/3))-
1));

h=(kg.*Nu_De)/(De);

Tbar= (Ti+Tw)/2; %at least for now. Wang does not define Tbar
anywhere

E_D                                                                =
2.86*(1+0.388.*Kn.*((Pe./Y).^(1/3))./((Y.^(1/3)).*(Pe.^(2/3)));
%brownian diffusion

N_R = ParticleDiameter/PoreDiameter; % eq 68

Stk=                                          ((ParticleDensity-
GasDensity).*((ParticleDiameter).^2).*ParticleVelocity)...
    ./(18* mu.* PoreDiameter); %stokes number eq59

E_I =.16*(N_R+(.5+.8*N_R).*Stk-.105*Stk.^2); %inertia eq 67

Re  =  GasDensity  *GasVelocity  *PoreDiameter/  mu;    %reynolds
number

H_tilde = 2-log(Re); %hydrodynamic factor eq 70

E_R              =              (N_R.*(N_R+1.996.*Kn))./(H_tilde
+1.996.*Kn.*(H_tilde+.5));
%direct interception eq 69

E_G = (ParticleDensity - rho)./...

(18.*mu.*SuperficialVelocity).*9.81.*((ParticleDiameter).^2);
%gravity effect, from Konstandopolous
```

```
E_T = ((Cc.*GasDensity.*Cp.*Re_De.*f.*Kth.*nu.*(Ti-Tw))./...
    (De.*h.*Tbar)).*(1-exp((-
Ca.*Peri.*h.*L)./(GasDensity*(Q*3600)*Cp)));

% E_DRI1=E_D+E_R+E_I; %simple sum

% alpha1= (4/pi).*((beta)./epsilon).*(w./PoreDiameter).*E_DRI1;

alpha2=
AC1.*((4/pi).*((beta)./epsilon).*(w./PoreDiameter).*(AC2.*E_D+E_
R+E_I))+...
    (((-3/4)*(beta)./CollectorDiameter/2)*E_G)+E_T;

% FilterEfficiency1=1-exp(-alpha1);
FilterEfficiency2=(1-exp(-alpha2));

%                                          loglog(ParticleDiameter,
(4/pi).*((beta)./epsilon).*(w./PoreDiameter).*E_D, ...
%
ParticleDiameter,(4/pi).*((beta)./epsilon).*(w./PoreDiameter)*
E_I, ...
%                                                ParticleDiameter,
(4/pi).*((beta)./epsilon).*(w./PoreDiameter).*E_R,...
%      ParticleDiameter, (-3/4)*(1-epsilon)*E_G, ...
%      ParticleDiameter, E_T, ...
%      ParticleDiameter, FilterEfficiency1);

% legend('DiffEff','IntEff','ImpEff', 'GravEff','ThermEff',...
%     'Filter Efficiency', 'Location', 'SouthWest');

 plot(ParticleDiameter*10^6, FilterEfficiency2);
 %axis([10 1000 0 1])

assignin('base','FilterEfficiency', FilterEfficiency2);
ExpectedRemovalEfficiency=mean(FilterEfficiency2);

Output=Utility(ExpectedRemovalEfficiency, ExpectedPressureDrop);
end

%end of file ShepFilter558
```

Simulation Model for Filters of 61.1% Porosity

```
function Output=ShepFilter611(Ti, Tw, Q)

%Q MUST be in m^3/sec
```

```
%the original thermophoresis programming expects Q to be m^3/hr,
so some
%conversions exists in those equations

epsilon=.611; %porosity
N=  45; %number of inlet channels,58
AC1=1; %for lowflow use AC1=1 and AC2=1.33
AC2=1.33;  % arbitrary constants for highflow use AC1=1 and
AC2=1.77
w= .3 *10^-3; %WallThickness; %variable

CollectorDiameter=23.83;

ParticleDiameter
=[20.9000000000000;21.7000000000000;22.5000000000000;...
    23.3000000000000;24.1000000000000;25;25.9000000000000;...
    26.9000000000000;27.9000000000000;28.9000000000000;30;...
    31.1000000000000;32.2000000000000;33.4000000000000;...
    34.6000000000000;35.9000000000000;37.2000000000000;...
    38.5000000000000;40;41.4000000000000;42.9000000000000;...
    44.5000000000000;46.1000000000000;47.8000000000000;...
    49.6000000000000;51.4000000000000;53.3000000000000;...
    55.2000000000000;57.3000000000000;59.4000000000000;...
    61.5000000000000;63.8000000000000;66.1000000000000;...
    68.5000000000000;71;73.7000000000000;76.4000000000000;...
    79.1000000000000;82;85.1000000000000;88.2000000000000;...
    91.4000000000000;94.7000000000000;98.2000000000000;...

101.800000000000;105.500000000000;109.400000000000;113.400000000
000;...
    117.600000000000;121.900000000000;126.300000000000;131;...

135.800000000000;140.700000000000;145.900000000000;151.200000000
000;...

156.800000000000;162.500000000000;168.500000000000;174.700000000
000;...

181.100000000000;187.700000000000;194.600000000000;201.700000000
000;...

209.100000000000;216.700000000000;224.700000000000;232.900000000
000;...
    241.400000000000;250.300000000000;259.500000000000;269;...

278.800000000000;289;299.600000000000;310.600000000000;322;...
    333.800000000000;346;358.700000000000;371.800000000000;...
```

```
385.400000000000;399.500000000000;414.200000000000;429.400000000
000;...

445.100000000000;461.400000000000;478.300000000000;495.800000000
000;...
    514;532.800000000000;552.300000000000;572.500000000000;...

593.500000000000;615.300000000000;637.800000000000;661.200000000
000;...
    685.400000000000;710.500000000000;736.500000000000;]*10^-9;
%meters
% ParticleDiameter=logspace(-2,1,300).*10^-6; %meters
%ParticlesIn=input(2,:);

PoreDiameter= 25*10^-6; %ceramic property D_f

%epsilon=.50; %porosity %variable

ChannelLength= 225*10^-3;  %channelLength; %variable
ChannelWidth= 2*10^-3; % cellWidth; %variable
L=ChannelLength;
Ca= L/(4*ChannelWidth); %ratio of wall length of heat transfer
to the
%perimeter of the cross section
De=ChannelWidth; %=4*A/P Hydraulic Diameter
Peri= 4*ChannelWidth;
GasVelocity = Q/(N*4*ChannelWidth*L);

yvan=1; %van der Waals scale
Cc =0.82*(((ChannelWidth/2)./yvan).^(1/7));

Pressure=  6894.76*14.7/1000;  %abs  exhaust  gas  pressure,  kPa,
parameter

B=1.38*10^-23; %Boltsman's constant J/Kelvin
MW=29; %molar weight of the fluid
R_uni=8.314; %universal gas constant
R= R_uni/MW; %exhaust specific gas constant,

GasDensity=Pressure/(R*Ti);

MW=29; % molar weight of fluid
Pa_per_psi=6894.76;
PascalPressure=Pressure*Pa_per_psi;
rho=MW*PascalPressure/1000/(R_uni*Ti);

Cp=3*(10^-7)*(Ti-273).^2    +    5*(10^-5)*(Ti-273)    +    1.0029;
%specific heat of the gas
```

```
kg= 7*(10^-5)*(Ti-273) + 0.0245; %thermal conductivity of gas
%Cp and kg relationships are a regression of data given at
%engineeringtoolbox.com. Not valid past 400C

kp= 5.4*(300/Ti).^(1.14); %thermal conductivity of particle,
%equation given in Clayton et al "Thermal-mechanical
%modeling of a generic high-level waste salt repository"
Mechanical
%Behavior of Salt VII - Proceedings of the 7th Conference on the
Mechanical
%Behavior of Salt, 2012, pp.435-439

SuperficialVelocity = Q/(N*4*ChannelWidth*L); %written as v_wall
in the paper
ParticleVelocity=SuperficialVelocity; %approximately true

ParticleDensity=(2165); %kg/m^3
%this is for sodium chloride %will be a function of particle
diameter

mu=1.846*10^-5; %dynamic fluid viscosity
nu=mu/GasDensity;

Permeability= ((PoreDiameter.^2).*epsilon.^(5.5))/(5.6);

gamm=  sqrt((48.*Permeability.*L.^2)./(w.*ChannelWidth.^3));  %eq
12

PressureDrop=((6*mu*L*Q)./(N*ChannelWidth.^4))*...
    (2*(exp(gamm)+1)+gamm.*(exp(gamm)-1))./(gamm.*(exp(gamm)-
1));

ExpectedPressureDrop=mean(PressureDrop);

lambda    =    mu/(0.499.*Pressure.*((8/(pi*(R/1000)*Ti)).^0.5));
%mean free path

Kn = 2.*lambda./PoreDiameter; %knudson number

beta = 1-epsilon; %packing density

H = .75-.5*log(beta);

Y = H+1.996*Kn*(H+.05);

D = B.*Ti./(3*pi*mu.*ParticleDiameter); %Diffusion Coefficient

Pe = ParticleVelocity.*PoreDiameter./D; %pecklet number
```

```
Re_De = GasVelocity *ChannelWidth/ nu;  %reynolds number

f=0.3164*Re_De.^(-.25);

lambda    =    mu/(0.499.*Pressure.*((8/(pi*(R/1000)*Ti)).^0.5));
%mean free path

Kn  =  2.*lambda./ChannelWidth;  %knudson  number,  not  explicitly
defined by Wang

Cu=     1+     (2*lambda./ParticleDiameter).*(1.257     +.4.*exp(-
.55*ParticleDiameter./lambda));
%Cunningham correction factor, coefficients for air


Kth                                                              =
(2.294.*((kg/kp)+2.2*Kn)*Cu)/((1+3.438*Kn)*(1+2*(kg/kp)+4.4*Kn))
;

Pr= 10^-09*(Ti-273).^3  -  3*10^-07*(Ti-273).^2  -  0.0001*(Ti-273)
+ 0.7174; %Prandtl Number
%generally  Pr=Cp.*mu./(kg),  but  this  gives  the  temperature
dependence. This
%relationship   is   a   regression   of   data   given   at
engineeringtoolbox.com.

Nu_De=((f/8)*(Re_De-1000)*Pr)/(1+12.7*sqrt(f/8)*((Pr.^(2/3))-
1));

h=(kg.*Nu_De)/(De);

Tbar=  (Ti+Tw)/2;  %at  least  for  now.  Wang  does  not  define  Tbar
anywhere

E_D                                                              =
2.86*(1+0.388.*Kn.*((Pe./Y).^(1/3))./((Y.^(1/3)).*(Pe.^(2/3)));
%brownian diffusion

N_R = ParticleDiameter/PoreDiameter; % eq 68

Stk=                                          ((ParticleDensity-
GasDensity).*((ParticleDiameter).^2).*ParticleVelocity)...
    ./(18* mu.* PoreDiameter); %stokes number eq59

E_I =.16*(N_R+(.5+.8*N_R).*Stk-.105*Stk.^2); %inertia eq 67

Re  =  GasDensity  *GasVelocity  *PoreDiameter/  mu;    %reynolds
number
```

```
H_tilde = 2-log(Re); %hydrodynamic factor eq 70

E_R               =               (N_R.*(N_R+1.996.*Kn))./(H_tilde
+1.996.*Kn.*(H_tilde+.5));
%direct interception eq 69

E_G = (ParticleDensity - rho)./...

(18.*mu.*SuperficialVelocity).*9.81.*((ParticleDiameter).^2);
%gravity effect, from Konstandopolous

E_T = ((Cc.*GasDensity.*Cp.*Re_De.*f.*Kth.*nu.*(Ti-Tw))./...
    (De.*h.*Tbar)).*(1-exp((-
Ca.*Peri.*h.*L)./(GasDensity*(Q*3600)*Cp)));

% E_DRI1=E_D+E_R+E_I; %simple sum

% alpha1= (4/pi).*((beta)./epsilon).*(w./PoreDiameter).*E_DRI1;

alpha2=
AC1.*((4/pi).*((beta)./epsilon).*(w./PoreDiameter).*(AC2.*E_D+E_
R+E_I))+...
    (((-3/4)*(beta)./CollectorDiameter/2)*E_G)+E_T;

% FilterEfficiency1=1-exp(-alpha1);
FilterEfficiency2=(1-exp(-alpha2));

%                                        loglog(ParticleDiameter,
(4/pi).*((beta)./epsilon).*(w./PoreDiameter).*E_D, ...
%
ParticleDiameter,(4/pi).*((beta)./epsilon).*(w./PoreDiameter)*
E_I, ...
%                                             ParticleDiameter,
(4/pi).*((beta)./epsilon).*(w./PoreDiameter).*E_R,...
%      ParticleDiameter, (-3/4)*(1-epsilon)*E_G, ...
%      ParticleDiameter, E_T, ...
%      ParticleDiameter, FilterEfficiency1);

% legend('DiffEff','IntEff','ImpEff', 'GravEff','ThermEff',...
%     'Filter Efficiency', 'Location', 'SouthWest');

 plot(ParticleDiameter*10^6, FilterEfficiency2);
 %axis([10 1000 0 1])

assignin('base','FilterEfficiency', FilterEfficiency2);
ExpectedRemovalEfficiency=mean(FilterEfficiency2);

Output=Utility(ExpectedRemovalEfficiency, ExpectedPressureDrop);
end
```

```
%end of file ShepFilter611
```

Simulation Model for Filters of 65.0% Porosity

```
function Output=ShepFilter650(Ti, Tw, Q)

%Q MUST be in m^3/sec
%the original thermophoresis programming expects Q to be m^3/hr,
so some
%conversions exists in those equations

epsilon=.650; %porosity
N=  60; %number of inlet channels, was 5765 (90 current)
AC1=1; %arbitrary constant for lowflow use AC1=1 and AC2=1.3
AC2=1.3; %arbitrary constant for highflow use AC1=1 and AC2=1.66
w= .3 *10^-3; %WallThickness; %variable

CollectorDiameter=23.83;

ParticleDiameter
=[20.9000000000000;21.7000000000000;22.5000000000000;...
    23.3000000000000;24.1000000000000;25;25.9000000000000;...
    26.9000000000000;27.9000000000000;28.9000000000000;30;...
    31.1000000000000;32.2000000000000;33.4000000000000;...
    34.6000000000000;35.9000000000000;37.2000000000000;...
    38.5000000000000;40;41.4000000000000;42.9000000000000;...
    44.5000000000000;46.1000000000000;47.8000000000000;...
    49.6000000000000;51.4000000000000;53.3000000000000;...
    55.2000000000000;57.3000000000000;59.4000000000000;...
    61.5000000000000;63.8000000000000;66.1000000000000;...
    68.5000000000000;71;73.7000000000000;76.4000000000000;...
    79.1000000000000;82;85.1000000000000;88.2000000000000;...
    91.4000000000000;94.7000000000000;98.2000000000000;...

101.800000000000;105.500000000000;109.400000000000;113.400000000
000;...
    117.600000000000;121.900000000000;126.300000000000;131;...

135.800000000000;140.700000000000;145.900000000000;151.200000000
000;...

156.800000000000;162.500000000000;168.500000000000;174.700000000
000;...

181.100000000000;187.700000000000;194.600000000000;201.700000000
000;...

209.100000000000;216.700000000000;224.700000000000;232.900000000
000;...
```

```
    241.400000000000;250.300000000000;259.500000000000;269;...

278.800000000000;289;299.600000000000;310.600000000000;322;...
    333.800000000000;346;358.700000000000;371.800000000000;...

385.400000000000;399.500000000000;414.200000000000;429.400000000
000;...

445.100000000000;461.400000000000;478.300000000000;495.800000000
000;...
    514;532.800000000000;552.300000000000;572.500000000000;...

593.500000000000;615.300000000000;637.800000000000;661.200000000
000;...
    685.400000000000;710.500000000000;736.500000000000;]*10^-9;
%meters
% ParticleDiameter=logspace(-2,1,300).*10^-6; %meters
%ParticlesIn=input(2,:);

PoreDiameter= 25*10^-6; %ceramic property D_f

%epsilon=.50; %porosity %variable

ChannelLength= 225*10^-3;  %channelLength; %variable
ChannelWidth= 2*10^-3; % cellWidth; %variable
L=ChannelLength;
Ca= L/(4*ChannelWidth); %ratio of wall length of heat transfer
to the
%perimeter of the cross section
De=ChannelWidth; %=4*A/P Hydraulic Diameter
Peri= 4*ChannelWidth;

GasVelocity = Q/(N*4*ChannelWidth*L);

yvan=1; %van der Waals scale
Cc =0.82*(((ChannelWidth/2)./yvan).^(1/7));

Pressure=  6894.76*14.7/1000;  %abs  exhaust  gas  pressure,  kPa,
parameter

B=1.38*10^-23; %Boltsman's constant J/Kelvin
MW=29; %molar weight of the fluid
R_uni=8.314; %universal gas constant
R= R_uni/MW; %exhaust specific gas constant,

GasDensity=Pressure/(R*Ti);

MW=29; % molar weight of fluid
Pa_per_psi=6894.76;
```

```
PascalPressure=Pressure*Pa_per_psi;
rho=MW*PascalPressure/1000/(R_uni*Ti);

Cp=3*(10^-7)*(Ti-273).^2    +    5*(10^-5)*(Ti-273)    +    1.0029;
%specific heat of the gas
kg= 7*(10^-5)*(Ti-273) + 0.0245; %thermal conductivity of gas
%Cp and kg relationships are a regression of data given at
%engineeringtoolbox.com. Not valid past 400C

kp= 5.4*(300/Ti).^(1.14); %thermal conductivity of particle,
%equation given in Clayton et al "Thermal-mechanical
%modeling  of  a  generic  high-level  waste  salt  repository"
Mechanical
%Behavior of Salt VII - Proceedings of the 7th Conference on the
Mechanical
%Behavior of Salt, 2012, pp.435-439

SuperficialVelocity = Q/(N*4*ChannelWidth*L); %written as v_wall
in the paper
ParticleVelocity=SuperficialVelocity; %approximately true

ParticleDensity=(2165); %kg/m^3
%this  is  for  sodium  chloride  %will  be  a  function  of  particle
diameter

mu=1.846*10^-5; %dynamic fluid viscosity
nu=mu/GasDensity;

Permeability= ((PoreDiameter.^2).*epsilon.^(5.5))/(5.6);

gamm=  sqrt((48.*Permeability.*L.^2)./(w.*ChannelWidth.^3));  %eq
12

PressureDrop=((6*mu*L*Q)./(N*ChannelWidth.^4))*...
    (2*(exp(gamm)+1)+gamm.*(exp(gamm)-1))./(gamm.*(exp(gamm)-
1));

ExpectedPressureDrop=mean(PressureDrop);

lambda    =    mu/(0.499.*Pressure.*((8/(pi*(R/1000)*Ti)).^0.5));
%mean free path

Kn = 2.*lambda./PoreDiameter; %knudson number

beta = 1-epsilon; %packing density

H = .75-.5*log(beta);

Y = H+1.996*Kn*(H+.05);
```

```
D = B.*Ti./(3*pi*mu.*ParticleDiameter); %Diffusion Coefficient

Pe = ParticleVelocity.*PoreDiameter./D; %pecklet number

Re_De = GasVelocity *ChannelWidth/ nu;  %reynolds number

f=0.3164*Re_De.^(-.25);

lambda    =    mu/(0.499.*Pressure.*((8/(pi*(R/1000)*Ti)).^0.5));
%mean free path

Kn  =  2.*lambda./ChannelWidth;  %knudson  number,  not  explicitly
defined by Wang

Cu=     1+     (2*lambda./ParticleDiameter).*(1.257     +.4.*exp(-
.55*ParticleDiameter./lambda));
%Cunningham correction factor, coefficients for air


Kth                                                              =
(2.294.*((kg/kp)+2.2*Kn)*Cu)/((1+3.438*Kn)*(1+2*(kg/kp)+4.4*Kn))
;

Pr= 10^-09*(Ti-273).^3  -  3*10^-07*(Ti-273).^2  -  0.0001*(Ti-273)
+ 0.7174; %Prandtl Number
%generally  Pr=Cp.*mu./(kg),  but  this  gives  the  temperature
dependence. This
%relationship   is   a   regression   of   data   given   at
engineeringtoolbox.com.

Nu_De=((f/8)*(Re_De-1000)*Pr)/(1+12.7*sqrt(f/8)*((Pr.^(2/3))-
1));

h=(kg.*Nu_De)/(De);

Tbar=  (Ti+Tw)/2;  %at  least  for  now.  Wang  does  not  define  Tbar
anywhere

E_D                                                              =
2.86*(1+0.388.*Kn.*((Pe./Y).^(1/3))./((Y.^(1/3)).*(Pe.^(2/3)));
%brownian diffusion

N_R = ParticleDiameter/PoreDiameter; % eq 68

Stk=                                          ((ParticleDensity-
GasDensity).*((ParticleDiameter).^2).*ParticleVelocity)...
    ./(18* mu.* PoreDiameter); %stokes number eq59
```

```
E_I =.16*(N_R+(.5+.8*N_R).*Stk-.105*Stk.^2); %inertia eq 67

Re = GasDensity *GasVelocity *PoreDiameter/ mu;    %reynolds
number

H_tilde = 2-log(Re); %hydrodynamic factor eq 70

E_R               =               (N_R.*(N_R+1.996.*Kn))./(H_tilde
+1.996.*Kn.*(H_tilde+.5));
%direct interception eq 69

E_G = (ParticleDensity - rho)./...

(18.*mu.*SuperficialVelocity).*9.81.*((ParticleDiameter).^2);
%gravity effect, from Konstandopolous

E_T = ((Cc.*GasDensity.*Cp.*Re_De.*f.*Kth.*nu.*(Ti-Tw))./...
    (De.*h.*Tbar)).*(1-exp((-
Ca.*Peri.*h.*L)./(GasDensity*(Q*3600)*Cp)));

% E_DRI1=E_D+E_R+E_I; %simple sum

% alpha1= (4/pi).*((beta)./epsilon).*(w./PoreDiameter).*E_DRI1;


alpha2=
AC1.*((4/pi).*((beta)./epsilon).*(w./PoreDiameter).*(AC2.*E_D+E_
R+E_I))+...
    (((-3/4)*(beta)./CollectorDiameter/2)*E_G)+E_T;

% FilterEfficiency1=1-exp(-alpha1);
FilterEfficiency2=(1-exp(-alpha2)); %needs to be a subratction
not a multiplier like this

%                                        loglog(ParticleDiameter,
(4/pi).*((beta)./epsilon).*(w./PoreDiameter).*E_D, ...
%
ParticleDiameter,(4/pi).*((beta)./epsilon).*(w./PoreDiameter)*
E_I, ...
%                                                ParticleDiameter,
(4/pi).*((beta)./epsilon).*(w./PoreDiameter).*E_R,...
%      ParticleDiameter, (-3/4)*(1-epsilon)*E_G, ...
%      ParticleDiameter, E_T, ...
%      ParticleDiameter, FilterEfficiency1);

% legend('DiffEff','IntEff','ImpEff', 'GravEff','ThermEff',...
%     'Filter Efficiency', 'Location', 'SouthWest');

 plot(ParticleDiameter*10^6, FilterEfficiency2);
```

```
 %axis([10 1000 0 1])

assignin('base','FilterEfficiency', FilterEfficiency2);
ExpectedRemovalEfficiency=mean(FilterEfficiency2);

Output=Utility(ExpectedRemovalEfficiency, ExpectedPressureDrop);
end

%end of file ShepFilter650
```

Permeability Calculations

```
function Permeability=Pressuredrop(Q,N,Pressuredrop)

WallThickness= .3 *10^-3; %m; %variable
ChannelWidth= 2*10^-3; % cellWidth; %variable
L= 225*10^-3;  %channelLength; %variable
SuperficialVelocity = Q/(N*4*ChannelWidth*L);

mu=1.85*10^-5; %dynamic fluid viscosity

Permeability=SuperficialVelocity.*mu.*WallThickness./(Pressuredr
op);

%end of file Permeability.m
```